

Synaptome architecture shapes regional dynamics in the mouse brain

Justine Y. Hansen¹, Andrea I. Luppi^{1,2}, Zhen Qiu^{3,4}, Silvia Gini⁵,

Ben D. Fulcher⁶, Alessandro Gozzi⁵, Seth G. N. Grant⁴, Bratislav Misic^{1,*}

¹Montréal Neurological Institute, McGill University, Montréal, QC, Canada

²Centre for Eudaimonia and Human Flourishing, Department of Psychiatry, University of Oxford, Oxford, UK

³School of Science and Engineering, University of Dundee, Dundee, UK

⁴Centre for Clinical Brain Sciences, University of Edinburgh, Edinburgh, UK

⁵Center for Neuroscience and Cognitive Systems, Istituto Italiano di Tecnologia, Rovereto, Italy

⁶School of Physics, The University of Sydney, Sydney, Australia

Synapses are the connections that transform neurons from simple electrically charged cells into complex circuits that support perception, cognition and action. Recent advances in single-punctum synapse mapping in mice have made it possible to study the diversity of synapses and how these synapse types are differentially expressed across the brain. A salient question is how synapse diversity shapes the spatial patterning of whole-brain dynamics. Here we derive $> 6\,000$ time-series features from fMRI recordings in awake mice to construct a comprehensive macroscale dynamical phenotype of each synapse type. We find that spatial variation in synapse types colocalizes with spatial variation in regional dynamics. Time-series in regions enriched for SAP102-expressing synapses display high-amplitude events while time-series in regions enriched for PSD95-expressing synapses display low stationarity. These regional variations in synapse types and dynamics are associated with patterns of structural and functional connectivity and the placement of hubs. Finally, using two additional fMRI datasets in anaesthetized mice, we show that synapses expressing short- and long-lifetime proteins are differentially engaged across behavioural states. Collectively, this work demonstrates that the spatial organization of microscale synapse types fundamentally shapes whole-brain dynamics.

INTRODUCTION

The brain is composed of billions of interconnected neurons that support the propagation of electrical signals and the emergence of cognition and behaviour. A fundamental unit in all neural circuits is the synapse. While hodology is typically focused on whether a synapse exists (i.e., whether two neurons are connected), a frequently overlooked question is what type of synapse is present, and how this synaptic phenotype shapes its function. Indeed, different excitatory synapses express different neurotransmitter receptors, ion channels, and signaling complexes [1, 6, 7]. This cocktail of synaptic proteins shapes the voltage dynamics of a single neuron [8–10]. In other words, brain function emerges not only from complex patterns of neural wiring, but also from the specific synaptic phenotype at every individual point of contact. Characterizing different synapse phenotypes, or synapse “types”, throughout the brain is necessary for understanding how regional synaptic architecture ultimately shapes regional brain dynamics and connectivity.

Recent single-punctum synapse mapping technology in mice has made it possible to image the proteomic composition of individual synapses throughout the whole brain, revealing an immense diversity of synapse types—the synaptome [1, 11]. Two synaptic proteins in particular are well-suited candidates for genetic tagging in mouse models: postsynaptic density 95 (PSD95) and synapse-associated protein 102 (SAP102). These two

postsynaptic scaffolding proteins are stably and abundantly expressed in excitatory synapses, assemble receptors, channels, and other signaling molecules into multiprotein signaling complexes, and play a direct role in shaping the synapse’s response to a neural signal [1, 8, 10]. PSD95 and SAP102 synapses can be further classified according to morphological features into multiple synapse subtypes, each with unique properties. For example, some synapse subtypes stably express PSD95 over multiple weeks (“long-lifetime” synapses), while other synapse subtypes recycle PSD95 within a matter of hours (“short-lifetime” synapses), a possible mechanism underlying memory, cognitive flexibility, and learning [2]. Furthermore, mice that do not express PSD95 or SAP102 demonstrate abnormal synaptic transmission, as well as cognitive and learning deficits that are specific to the type of synapse that is affected [8–10, 12]. Importantly, synapses that express only PSD95 versus those that express only SAP102 are differentially expressed in the brain, such that each brain region has its own unique synaptic composition or synaptome architecture [1, 11].

The regional heterogeneity of synaptome architecture suggests that different brain regions are equipped to generate different patterns of neural dynamics. Indeed, whole-brain recordings of neural dynamics in mice consistently demonstrate spatial variation in local spontaneous activity [13, 14]. These patterns of dynamics are highly structured: they can be organized into networks of distributed areas with similar function [15–18], and change depending on behavioural state [4, 19]. Furthermore, recent data-driven feature extraction software has made it possible to comprehensively describe, using thousands of statistical time-series features, a rich dy-

* bratislav.misic@mcgill.ca

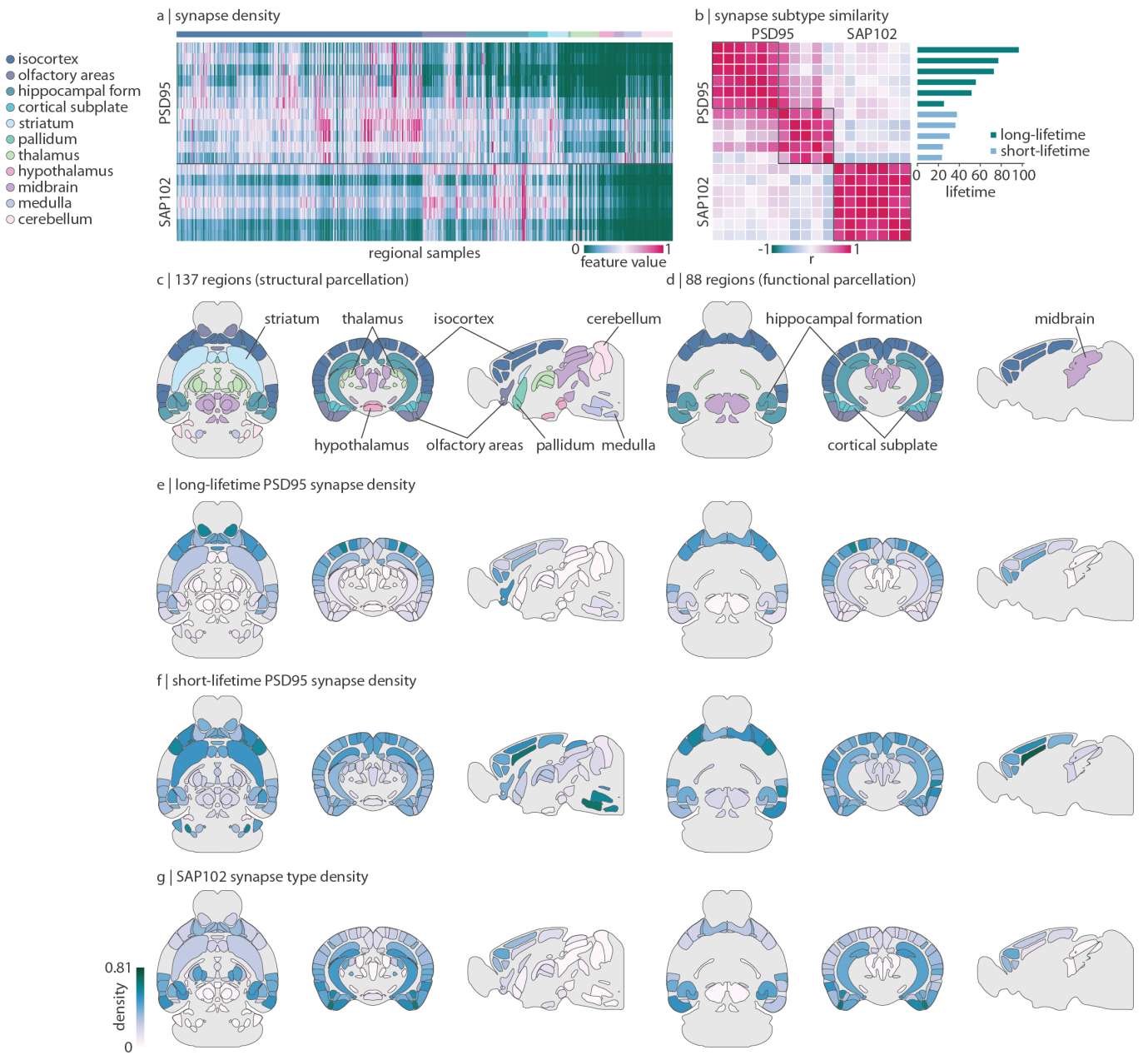


Figure 1. Synapse type density in the mouse brain | PSD95 and SAP102, two postsynaptic scaffolding proteins expressed at excitatory synapses, were fluorescently imaged at single-punctum resolution across the whole mouse brain [1]. (a) Normalized synapse density across 775 regional samples as presented in Zhu et al. [1]. PSD95-expressing synapses are divided into 11 subtypes and SAP102-expressing synapses into 7 subtypes, according to morphological parameters (rows). Regions are ordered according to major ontological structure (columns), as indicated by the horizontal bar. (b) Heatmap: pairwise correlation (Spearman's r) of synapse subtype density across regions. Barplot: protein lifetime of all 11 PSD95 subtypes [2]. Green bars indicate PSD95 subtypes that fall into the first cluster of highly coexpressed subtypes (deemed “long-lifetime PSD95 synapses”) and blue bars indicate PSD95 subtypes that fall into the second cluster (“short-lifetime PSD95 synapses”). (c) Axial, coronal, and sagittal view of the 137-region parcellation used for analyses involving tract-tracing data [3]. Note that tract-tracing data is limited to the right hemisphere although we show both hemispheres (mirrored). (d) Axial, coronal, and sagittal view of the 88-region parcellation used for analyses involving fMRI data [4]. Regions in panels (c) and (d) are coloured and labeled according to ontological structure. (e-g) Axial, coronal, and sagittal view of mean long-lifetime PSD95 synapse density (e), mean short-lifetime PSD95 synapse density (f), and mean SAP102 synapse density (g), mapped to both 137- and 88-region parcellations. The colourbar in (g) applies to all three panels e-g. All mouse brains are plotted using brainglobe-heatmap [5].

namical phenotype of every brain region [18, 20, 21]. What then are the mechanistic origins of these regionally heterogeneous dynamical phenotypes?

In the present report, we ask whether the dynamical phenotype of a brain region can be traced back to its underlying synaptic phenotype. Using whole-brain quantifications of PSD95- and SAP102-expressing synapses in the mouse brain, alongside resting-state functional magnetic resonance imaging (fMRI) recordings, we compare the spatial distribution of synapse types to $> 6\,000$ features of regional fMRI time-series. After establishing that each synapse type is associated with specific dynamics, we test whether a region's synaptic profile influences its embedding in global structural and functional networks. We then ask whether the functional role of a synapse type is ubiquitous across awake and anaesthetized behavioural states, or whether some synapses play a larger role during wakefulness. Finally, in multiple sensitivity and robustness analyses, we (1) validate synapse density maps in an independent dataset, (2) confirm our findings are not driven by fMRI signal-to-noise ratio (SNR), (3) confirm signal amplitude and time-series features do not reflect in-scanner motion, and (4) confirm our findings are not driven by the spatial localization of different cell types. Throughout, we find that the differential expression of synapse types maps onto unique features of macroscale neural dynamics and interregional connectivity.

RESULTS

Approximately one billion individual synaptic puncta were imaged in a whole mouse brain, using fluorescent markers for two synaptic proteins: PSD95 and SAP102 [1]. Morphological features (e.g. size, shape) of all PSD95- and SAP102-exclusively expressing synapses were quantified and clustered into 11 subtypes of PSD95 synapses and 7 subtypes of SAP102 synapses. Synapse density for these 18 synapse subtypes are mapped to 775 regions of the Allen Reference Atlas (ARA) [23] (Fig. 1a). By clustering the synapse density similarity matrix, defined as the Spearman correlation across brain regions of every pair of synapse subtypes, we find that all SAP102 synapse subtypes are similarly spatially expressed (Fig. 1b). For PSD95 synapses, we find two clusters of expression profiles that align nearly perfectly with the recycling rate of PSD95 within the synapse—that is, PSD95 lifetime (Fig. 1b barplot; see *Methods* for details on lifetime quantification; note that lifetime quantification was not performed for SAP102) [2]. We therefore separately analyze long-lifetime PSD95 synapses (6 subtypes; primarily shown in the main text) and short-lifetime PSD95 synapses (5 subtypes; primarily shown in the supplement).

To integrate the synapse density data with structural (tract-tracing) and functional (fMRI) datasets, we map the 775 samples to the regions included in the structural

(137 right hemisphere regions) and functional (88 bilateral regions) data (Fig. 1c–d, Fig. S1). For each synapse type—long-lifetime PSD95, short-lifetime PSD95, and SAP102—we show their average spatial expression profile on an axial, coronal, and sagittal view of the mouse brain (Fig. 1e–g). All synapse types are more populated in anterior regions such as the isocortex, cortical subplate, and olfactory areas. Long-lifetime PSD95 and SAP102 synapses demonstrate opposing dorsal-ventral density gradients in the coronal slice, with long-lifetime PSD95 synapses being more populated dorsally and SAP102 synapses being more populated ventrally. Short-lifetime PSD95 synapse density is highest in the medulla but otherwise relatively uniform across isocortical, olfactory, and subplate areas.

Synapse types are associated with unique macroscale dynamics

At the level of an individual synapse, its molecular make up and morphology is associated with a unique physiological response [8, 10], but does whole-brain synapse density map onto unique features of brain activity? To address this question, we apply recorded spontaneous fMRI activity in awake mice ($N = 10$), and compare regional variation in neural dynamics to regional variation in synapse types. Fig. 2 shows example time-series from brain regions with progressively more long-lifetime PSD95 synapse density (Fig. 2a) and SAP102 synapse density (Fig. 2b; time-series at the bottom are from regions with the greatest density). Visually, we observe that these BOLD signals are qualitatively different (Fig. 2a–b). Namely, time-series in regions with greater long-lifetime PSD95 synapse density appear less periodic and more variable than regions with lower long-lifetime PSD95 synapse density (Fig. 2a). Likewise, time-series in regions with high SAP102 synapse density show high-amplitude events (Fig. 2b).

While this initial visual inspection hints at potential relationships between synapse density and time-series properties, we turn to time-series analysis methods to comprehensively phenotype the dynamic signature of each brain region. Specifically, we use the highly comparative time-series analysis toolbox (htcsa) to compute 6 471 statistical features of each time-series in every region and mouse, including measurements of autocorrelation, entropy, frequency composition, signal amplitude distribution, and predictability [20, 21]. Features are then averaged across mice (Fig. 2c). Next, we correlate (Spearman's r) each synapse type with all 6 471 time-series features (Fig. 2d). This generates a list of time-series features that are significantly correlated with each synapse type (Bonferroni-corrected; Supplementary Table S1). Within each list, many time-series features measure similar phenomena; we therefore select a representative time-series feature that best summarizes each list (Fig. S2a, Fig. S3a; see *Methods* for details).

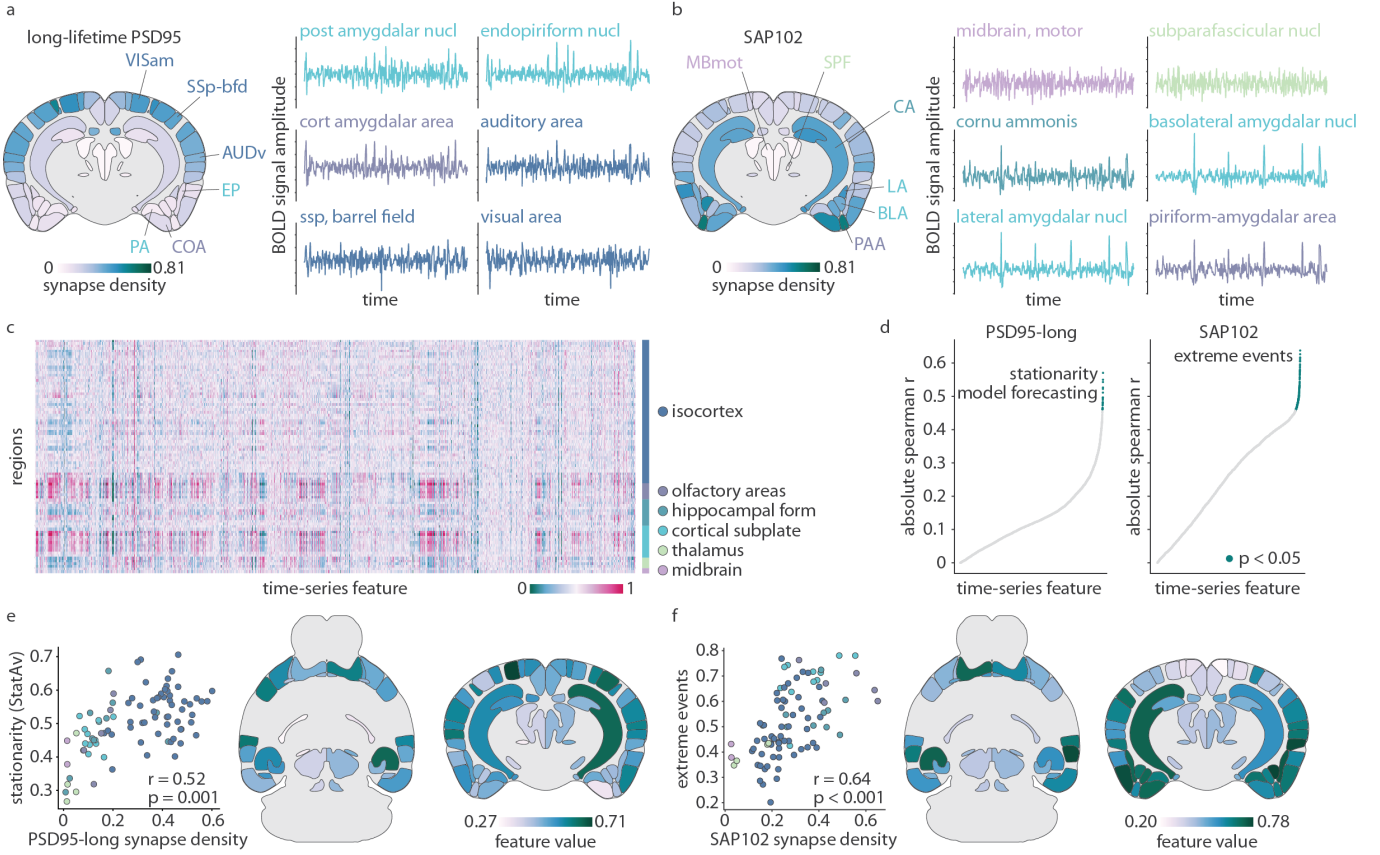


Figure 2. Synapse types are associated with unique macroscale dynamics | Resting-state awake fMRI data was acquired in 10 mice and time-series properties were correlated with synapse type densities. (a–b) Six example time-series from brain regions with variable long-lifetime PSD95 (a) and SAP102 (b) synapse density. Synapse density is shown on a coronal slice with the example brain regions labelled. Time-series colour indicates the region's major ontological structure (legend in panel (c)). (c) Using hctsa, > 6000 time-series features were calculated for each of 88 regional time-series in all mice. Time-series feature values were normalized to the unit interval, averaged across mice, and are shown in the heatmap. Brain regions are ordered according to ontological structure, as indicated by the vertical bar. (d) Each time-series feature was correlated (Spearman's r) with synapse density, for long-lifetime PSD95 and SAP102 synapses separately. Green points indicate statistical significance after multiple comparisons correction ($p < 0.05$, Bonferroni-corrected). Key features are labeled. (e) Scatter plot showing the correlation between long-lifetime PSD95 synapse density and StatAv₁₀, a measure of stationarity (standard deviation of the mean value of ten equally-sized time-series segments; greater value indicates greater standard deviation so lower stationarity; Fig. S2 [22]). (f) Scatter plot showing the correlation between SAP102 synapse density and the timing of extreme events in a time-series (Fig. S3). All mouse brains are plotted using brainglobe-heatmap [5].

We find that long-lifetime PSD95 synapse density is most correlated with features related to signal stationarity, such that regions with more long-lifetime PSD95 synapses have lower stationarity and more variable signal. Indeed, the cluster of features that are most correlated with long-lifetime PSD95 synapse density can be summarized by a simple statistic called StatAv₁₀ [22], which is defined as the standard deviation of n time-series segment means (Fig. S2b). Fig. 2e shows the correlation between long-lifetime PSD95 synapse density and StatAv₁₀ (StatAv over 10 non-overlapping time-series segments; $r = 0.52$, Bonferroni-corrected $p = 0.001$). Meanwhile, SAP102 synapse density is most correlated with features related to the presence

and timing of extreme (outlier) events, such that regions with more SAP102 synapses tend to demonstrate more high-amplitude events, especially later in the time-series. In Fig. 2f we show the correlation between SAP102 synapse density and a time-series feature that measures the median timing of extreme outlier events ($r = 0.64$, Bonferroni-corrected $p < 0.001$; see Fig. S3b for a deeper intuition of this representative time-series feature). Lastly, while we do repeat these analyses for short-lifetime PSD95 synapses (Fig. S4), we find a poor alignment between synapse density and time-series features, suggesting that short-lifetime PSD95 synapses are not reliably associated with specific features of neural dynamics.

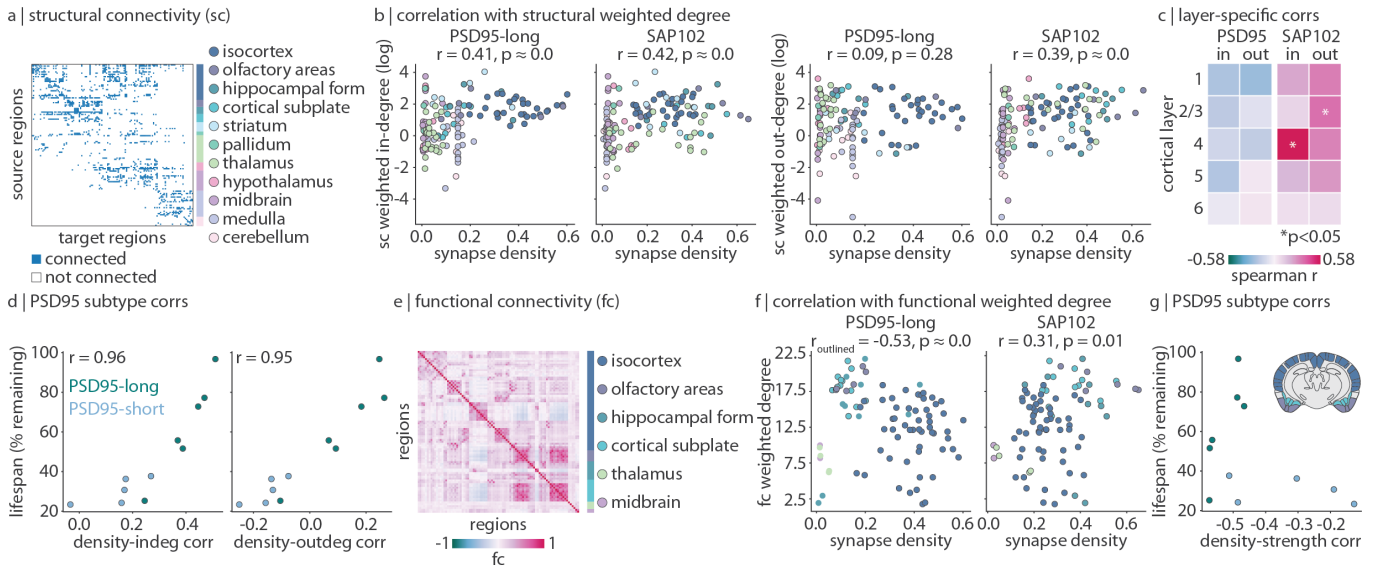


Figure 3. Synapse types colocalize with structural and functional hubs | (a) Structural connectivity matrix from tract-tracing data [3]. The matrix is binarized for visualization. (b) Correlations between long-lifetime PSD95 or SAP102 synapse density and weighted in- or out-degree of structural connectivity (sum of all afferent or efferent connections to or from a brain region, respectively). Weighted degree (*y*-axis) is log-transformed for visualization. Each point is a brain region, and regions are coloured according to their ontological structure. (c) Synapse density within each of 5 layers in the isocortex were separately correlated with weighted in- and out-degree. Asterisks represent $p < 0.05$. (d) Synapse density for each of 11 PSD95 synapse subtypes were correlated with weighted in- and out-degree of SC. Scatter plots show the density-degree correlation (Spearman's r) on the *x*-axis and PSD95 subtype lifetime on the *y*-axis. Each point represents a PSD95 subtype, and points are coloured according to whether they fall into the “long-lifetime” cluster or the “short-lifetime” cluster, as in Fig. 1b. (e) Average functional connectivity (Pearson's r) between pairs of regional time-series) across all mice. (f) Correlations between long-lifetime PSD95 or SAP102 synapse density and weighted degree of functional connectivity (sum of functional connectivity between one region and all other regions). Each point is a brain region, and regions are coloured according to their ontological structure. In the left-most scatter plot, only isocortical, olfactory, and cortical subplate regions are outlined and included in the correlation calculation. (g) Density-strength correlation (*x*-axis) versus synapse lifetime (*y*-axis) for all 11 PSD95 subtypes, as in panel (d). Note that the correlations are calculated using isocortical, olfactory, and cortical subplate regions only (ontological structures coloured in the coronal slice inset).

Synapse types colocalize with structural and functional hubs

Do synapse types—with their unique dynamic properties—make distinct macroscale structural and functional connections? Using a dataset of axonal projections in the mouse brain (Allen Mouse Brain Connectivity Atlas [3]), we constructed a 137×137 weighted and directed structural connectivity matrix (Fig. 3a). First we ask whether synapse density is correlated with structural weighted in-degree, that is, the sum of all afferent connection strengths into a single region. Since PSD95 and SAP102 are expressed postsynaptically, they are inherently markers of afferent connections. Indeed, despite their having distinct spatial expression profiles, we find that both long-lifetime PSD95 and SAP102 synapses are significantly positively correlated with weighted in-degree (long-lifetime PSD95: $r = 0.41, p < 0.001$; SAP102: $r = 0.42, p < 0.001$; Fig. 3b, left). Meanwhile, only SAP102 synapses—that is, those that mark high-amplitude events in the time-series—are significantly correlated with weighted out-degree (sum of

all efferent connection strengths; long-lifetime PSD95: $r = 0.09, p = 0.28$; SAP102: $r = 0.39, p \approx 0$; Fig. 3b, right). Short-lifetime PSD95 synapses again show poor alignment between synapse density and degree (in-degree: $r = 0.18, p = 0.03$; out-degree: $r = -0.16, p = 0.07$). One possible explanation for this dichotomy between synapse type and relationship with anatomical connectivity is that only some synapses generate the necessary dynamics needed for the neuron to establish axonal connections.

Global anatomical connectivity is also correlated with SAP102 synapse density—and not correlated with PSD95 synapse density—when we consider layer-specific synapse density in the isocortex (maximum 31 regions). By correlating weighted in- and out-degree with layer-specific synaptic densities, we find that only layer-specific SAP102 synapse density is significantly correlated with structural degree. SAP102 synapse density in layer IV—the primary recipient of afferent connections—is significantly correlated with weighted in-degree ($r = 0.58, p = 0.023$) and SAP102 density in layer II/III—the main source of cortico-cortical efferent connections—is

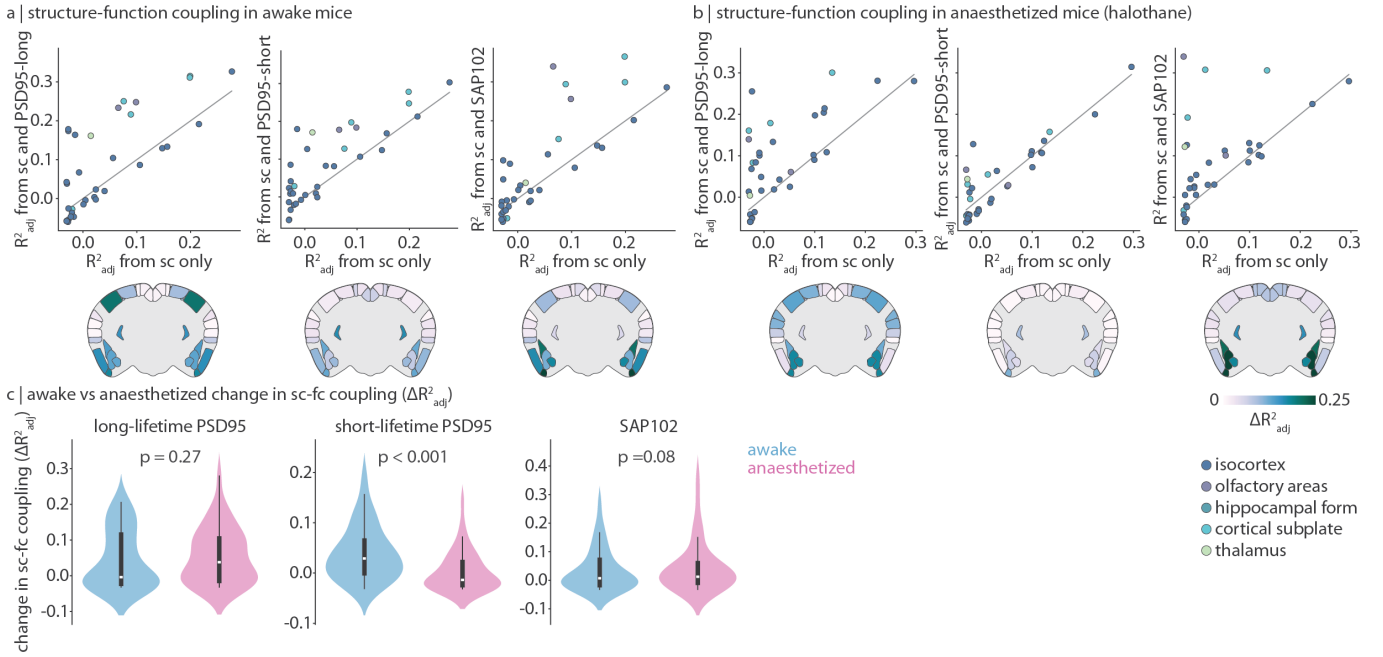


Figure 4. Synapse type density improves structure-function coupling | For each brain region, we predict its functional connectivity profile from either regional communicability alone (a measure of structural connectedness) or regional communicability alongside synapse type density. Structure-function coupling is defined as the fit (R^2_{adj}) of the model. (a–b) Using functional connectivity from awake (a) or anaesthetized (with halothane; b) mice, we calculate structure-function coupling before (x -axis) and after (y -axis) adding synapse type density (long-lifetime PSD95, short-lifetime PSD95, or SAP102) to the model. Each point is a brain region, and points are coloured according to major ontological structure. The identity line is shown in grey. Coronal slices show the change in coupling (ΔR^2_{adj}) after adding synapse density to the model. Data are mirrored across hemispheres for visualization. (c) We compare the change in structure-function coupling (distribution of ΔR^2_{adj}) in awake versus anaesthetized mice, for all three synapse types separately. Statistical significance is assessed using a two-sided dependent non-parametric t-test for paired samples (Wilcoxon signed-rank test). Violin plots estimate a kernel density on the underlying data, the white point represents the median, the thick vertical line represents the quartiles of the distribution, and the thin vertical line represents the range. All mouse brains are plotted using brainglobe-heatmap [5].

significantly correlated with weighted out-degree ($r = 0.36$, $p = 0.049$; Fig. 3c). Furthermore, we find that the correlation between PSD95 synapse density and structural degree is closely related to synapse lifetime: synapses with longer lifetime are more positively correlated with structural in- and out-degree ($r = 0.96$ for weighted in-degree, $r = 0.95$ for weighted out-degree; Fig. 3d).

We next compare synapse density with functional connectivity (pairwise correlation between regional fMRI time-series). Specifically, we correlate synapse density with regional weighted degree of functional connectivity, a measure of functional integration (defined as the sum of functional connectivity strengths between one region and all others; Fig. 3f). We find that short-lifetime PSD95 synapses are not correlated ($r = -0.08$, $p = 0.46$), and SAP102 synapses are weakly correlated ($r = 0.31$, $p = 0.01$), with functional weighted degree. On the other hand, long-lifetime PSD95 synapse density within cortical (isocortical, olfactory, and cortical subplate) structures is negatively correlated with functional weighted degree ($r = -0.53$, $p \approx 0$). In other words, regions with

fewer long-lifetime PSD95 synapses (and more stationary signal) tend to be functional hubs. Indeed, regions with many long-lifetime PSD95 synapses (and less stationary signal) are located in functionally specialized regions such as visual, somatosensory, and auditory cortex (Fig. 1e). Again, when we consider the 11 PSD95 subtypes individually, we find that all long-lifetime PSD95 synapses are correlated at $r \approx -0.5$ ($-0.57 \leq r \leq -0.45$) with functional weighted degree, whereas short-lifetime PSD95 synapse correlation coefficients range from -0.52 to -0.14 (Fig. 3g). Collectively, these findings demonstrate a dichotomy between long-lifetime PSD95 and SAP102 synapses: PSD95 synapses may be important for regional functional specialization, and SAP102 synapses may be involved in establishing a stable wiring architecture in the brain. In other words, the synaptic makeup of a region may shape its dynamical features and ultimately its embedding in large-scale networks.

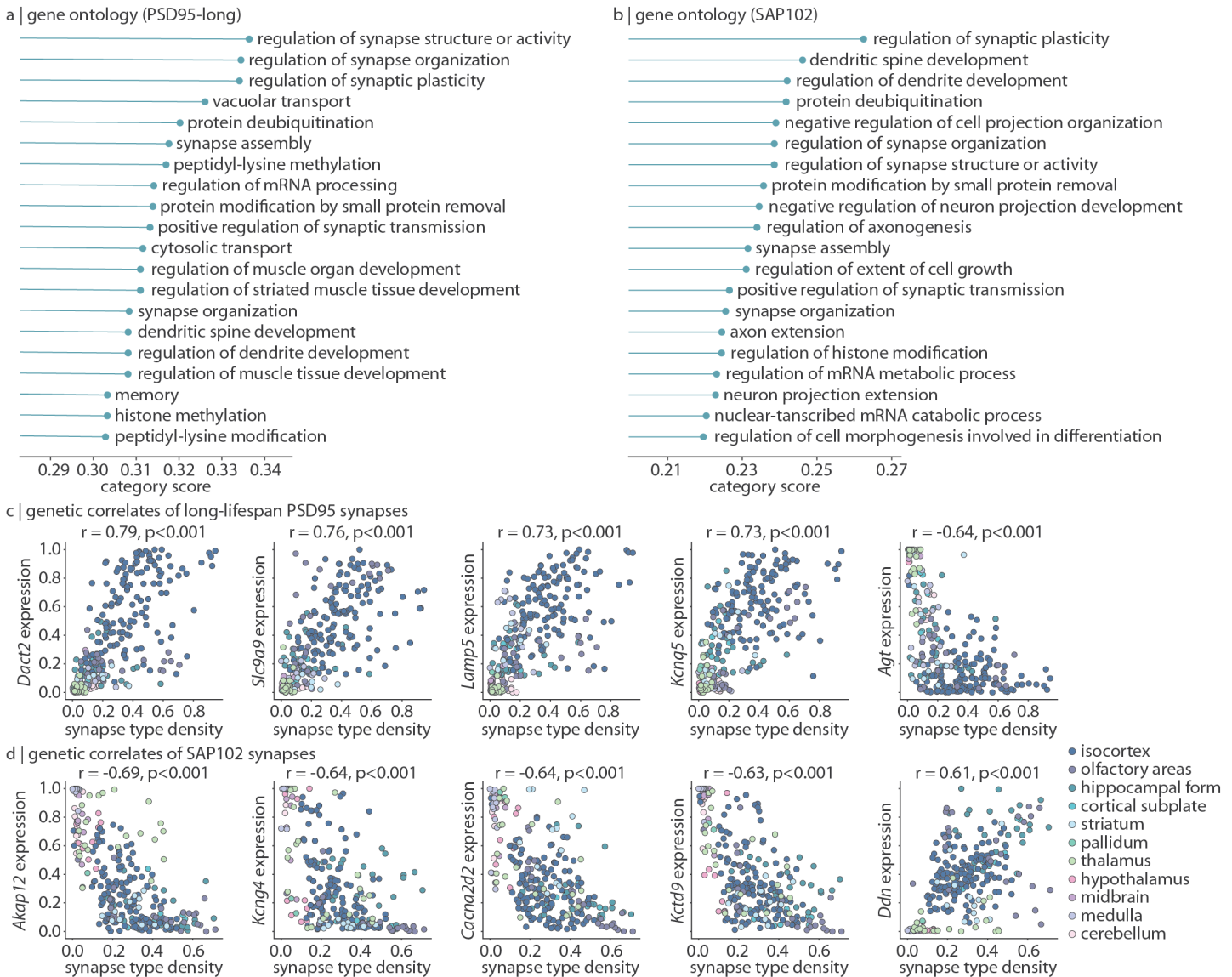


Figure 5. Transcriptomic profiling of synapse types | Gene expression data was acquired from the Allen Mouse Brain Atlas and correlated with synapse type density. (a–b) For each of 1 616 biological process categories associated with at least 100 genes, we calculate the median absolute correlation (Spearman's r) between long-lifetime PSD95 (a) or SAP102 (b) synapse density and all genes in the category (“category score”, x -axis). The top 20 category scores for each synapse type are shown. (c–d) Selected genes whose expression is highly correlated (Spearman's r) with long-lifetime PSD95 (c) or SAP102 (d) synapse density. Each point is a brain region ($N = 275$) and are coloured according to major ontological structure.

Synapse types mediate structure-function relationships

Given that structural and functional organization reflects synaptic architecture, we next ask whether synapse types mediate the coupling between brain structure and function [24, 25]. We define regional structure-function coupling as the fit (R_{adj}^2) of a simple linear regression model that predicts a region’s functional connectivity profile from its structural connectivity profile [26–29]. To bypass the limitation that structural connectivity is a sparse matrix, we calculate the communicability of the struc-

tural connectome, which results in a full matrix describing how easily information diffuses from one region to another. Next, we add either long-lifetime PSD95, short-lifetime PSD95, or SAP102 synapse density to the regression model and compare how model fit changes. This analysis is conducted using the 35 right hemisphere brain regions present in the structural, functional, and synapse density datasets. In Fig. 4a we show scatter plots where each point represents a brain region, the x -axis represents structure-function coupling when using structural connectivity alone, and the y -axis represents structure-

function coupling when synapse density is included in the model. As expected, most points, especially those representing non-isocortical regions, lie above the identity line (grey line in Fig. 4a; see coronal slices in Fig. 4a for change in coupling ($\Delta R_{\text{adj}}^2 > 0$)).

Thus far, short-lifetime PSD95 synapses consistently demonstrate weak or no correlation with features of macroscale neural dynamics, anatomical connectivity, and functional connectivity (Fig. S4). These synapses may house proteins with too quick a recycling rate to establish long-term dynamics (that can be measured with fMRI) or connections. We hypothesize that these short-lifetime PSD95 synapses, in comparison to long-lifetime PSD95 and SAP102 synapses, may be more relevant for the cognitive flexibility required when awake versus anaesthetized. We therefore extend our analyses to a dataset of fMRI recordings acquired on mice anaesthetized with halothane ($N = 19$; see *Methods* for details). We ask: does short-lifetime PSD95 synapse density only improve structure-function coupling when mice are awake?

Specifically, we recompute structure-function coupling before and after the addition of the three synapse types using a functional connectivity matrix derived from anaesthetized mice (Fig. 4b). We then compare how the addition of synapse type changes the regional distribution of ΔR_{adj}^2 for awake versus anaesthetized mice (Fig. 4c). For long-lifetime PSD95 and SAP102 synapses, structure-function coupling increases are not significantly different in anaesthetized versus awake mice (Wilcoxon signed-rank $p > 0.05$). Short-lifetime PSD95 synapses on the other hand demonstrate a significantly reduced ΔR_{adj}^2 in anaesthetized mice, that is, short-lifetime PSD95 synapse density information improves structure-function coupling significantly more in awake versus anaesthetized mice (Wilcoxon signed-rank $p < 0.001$). Finally, to ensure generalizability across different anaesthetics, we replicate these findings using a separate dataset of mice anaesthetized with a combination of medetomidine and isoflurane ($N = 14$, Fig. S5).

Sensitivity and robustness analysis

In this final subsection, we conduct four analyses to gauge the sensitivity and robustness of the current findings: (1) we validate synapse density measurements using an independent dataset, (2) we confirm our findings are not driven by fMRI SNR, (3) we ensure fMRI signal amplitude and time-series features are not driven by motion, and (4) we confirm that these results are specific to synapse types as opposed to spatial variation in cell types. First, PSD95 and SAP102 synapse density are derived from a single male mouse, raising the concern that these synapse density maps are specific to the individual. We therefore use gene expression data from *in situ* hybridization experiments in the Allen Mouse Brain Atlas to test whether synapses measured in a sin-

gle mouse are coexpressed with synaptic genes measured across multiple mice [23]. We correlate synapse type density with expression levels of 19 919 genes across 275 unique brain regions. Next, we summarize the biological processes of genes that are most coexpressed with each synapse type using a Gene Ontology analysis (see *Methods* for details). Despite long-lifetime PSD95 and SAP102 synapses following largely independent expression patterns ($r = 0.22$ in this 275-region parcellation), all three demonstrate greatest coexpression with genes involved in synaptic organization, plasticity, and development (Fig. 5a–b, Fig. S6a).

Furthermore, among the 1 295 most stably and reproducibly expressed genes, we find that all synapse types are again highly coexpressed with synaptic genes (Fig. 5c–d, Fig. S6b). For example, long-lifetime PSD95 synapse density is highly correlated with genes such as *Dact2* (involved in neural development and synapse formation; $r = 0.79$), *Slc9a9* (regulates ion balance across intracellular membranes; $r = 0.76$), *Lamp5* (regulates inhibitory synaptic transmission; $r = 0.73$), and multiple *Kcn* genes (potassium channel subunit genes, e.g. *Kcnq5*; $r = 0.73$). Likewise, SAP102 synapses are highly expressed with genes encoding synaptic proteins such as *Akap12* (scaffolding protein involved in signal transduction; $r = -0.69$), *Kcng4* and *Kctd9* (voltage-gated potassium channels; $r = -0.64$, $r = -0.63$, respectively), *Cacna2d2* (voltage-gated calcium channel; $r = -0.64$), and *Ddn* (Dendrin, a postsynaptic protein thought to be involved in retrograde signaling).

Second, we ensure that the relationship between synapse density and dynamics isn't driven by fMRI SNR. SNR was calculated as the mean signal within a voxel divided by the standard deviation of the signal outside of the brain mask, then parcellated to each of the 88 regions of interest. We correlate fMRI SNR with all time-series features used in the analyses, and find that 2 454 time-series features are significantly correlated with SNR ($p < 0.05$, Bonferroni-corrected). We therefore regress SNR from these 2 454 time-series features and repeat the analysis in Fig. 2d (Fig. S7a–b). We find that the dynamical phenotypes of both long-lifetime PSD95 and SAP102 synapses are replicable after removing the effects of fMRI SNR. More specifically, the dynamical phenotype of long-lifetime PSD95 synapses is still characterized by measures of stationarity, including *StatAv10* (Fig. S7c), and the dynamical phenotype of SAP102 synapses is still characterized by measures of the timing of extreme events, including *DN_OutlierInclude_n_001_mrrmd* (Fig. S7d).

Third, to ensure that the relationship between synapse density and dynamics is not driven by motion, we correlate every regional time-series with frame-wise displacement (FD; sum of absolute translational and rotational displacement between consecutive points in time; Fig. S8). A large correlation would indicate that signal amplitude reflects motion. Across all ten mice and 88 brain regions per mouse, the range of correlations

is $(-0.17, 0.24)$, and the median is 0.03. Therefore, we do not find evidence that signal amplitude is driven by motion. Furthermore, regions with high long-lifetime PSD95 synapse density and more non-stationary signal are regions with smaller correlations between motion and FD (correlation between long-lifetime PSD95 synapse density and average correlation between signal amplitude and FD: $r = -0.45$). Likewise, regions with high SAP102 synapse density and distinctive peaks in signal amplitude do not demonstrate greater correlations with FD ($r = 0.09$).

Fourth, we test the specificity of the relationship between synapse type and time-series features. In this report, we find evidence that long-lifetime PSD95 synapses are associated with signal stationarity, and SAP102 synapses are associated with the timing and presence of signal outliers. But are synapse types simply coexpressed with specific cellular populations that themselves induce these dynamics? To address this question, we correlate all three synapse types with the density of 9 different cell types (neurons, glia, excitatory neurons, inhibitory neurons, modulatory neurons, astrocytes, oligodendrocytes, microglia, and all cells; Fig. S9). Long-lifetime PSD95 synapses are significantly correlated with microglia density ($r = 0.49, p = 0.008$) and SAP102 synapses are significantly correlated with neurons ($r = 0.46, p = 0.012$) and excitatory neurons ($r = 0.60, p = 0.0001$). However, microglia density is only correlated with seven time-series features related to signal scaling, neuron density is not significantly correlated with any time-series features, and excitatory neuron density is only significantly correlated with a single time-series feature related to signal entropy. We therefore conclude that the reported associations between synapse type and regional dynamics are not driven by the spatial localization of specific cells.

DISCUSSION

In the present study, we find that different properties of neural activity can be traced back to the expression of specific synapse types. As a result, the synaptic composition of a brain region not only shapes its macroscale dynamics but also its embedding in whole-brain structural and functional networks. Synapse lifetime emerges as an important property of the synapse, whereby long-lifetime synapses tend to be related to brain connectivity while short-lifetime synapses are involved in functional processing during wakefulness. Altogether, this work bridges the microscale and the macroscale in describing synaptic influence on whole-brain dynamics and connectivity.

The present report is part of a broader effort to understand how different synapses shape brain function. Although synapses are traditionally thought to belong to one of three groups (excitatory, inhibitory, modulatory), mass spectrometry and immunoblotting experiments have revealed an enormous diversity of synaptic

proteins and synaptic functions [1, 7, 30]. Here we focus on two types of excitatory synapses: those that express PSD95 and those that express SAP102. These two proteins are differentially expressed throughout the brain and have different effects on the synapse [1]. While the structure and function of individual synapse types have been described [10, 31, 32], their macroscale impact is less well understood [1, 12]. The fundamental question that we address is: is the synaptic make-up of a brain region related to its functional dynamics?

There is a rich body of literature aimed at understanding the molecular and cellular origins of neural dynamics [33–35]. Previous studies have reported that neural oscillations may emerge from specific cell types [36], local gene transcription [37], or neurotransmitter receptors [38]. However, these findings are based only on a small number of time-series features. To address this limitation, new feature engineering methods have been developed to make it possible to comprehensively summarize the statistical features of an activity time-course [20, 21]. Using such an approach, recent work has demonstrated that different properties of neural dynamics can be traced back to specific elements of brain organization, including anatomical wiring [18], cell type distributions [39], and myelination [40], although how these layers of brain organization modulate dynamics is still unclear.

One overlooked yet compelling molecular feature that likely modulates neural dynamics is the synapse [34]. Here we compare regional dynamical phenotypes to the underlying expression of different synapses and find that each synapse type is associated with specific features of brain activity. PSD95 synapses are enriched in regions with non-stationary dynamics and SAP102 synapses are enriched in regions whose dynamics are marked by high-amplitude events. This suggests that SAP102 synapses are tuned to perfectly timed input stimuli that result in a burst of activity, whereas PSD95 synapses are responsive to a wide range of inputs, resulting in a more random pattern of excitatory postsynaptic potentials, firing rate, and macroscale neural dynamics. Indeed, our finding is consistent with reports from single-synapse pharmacological experiments that show that PSD95 synapses are involved in synapse strengthening regardless of the input stimulus frequency [8], whereas SAP102 synapses are frequency-specific in their modulation of plasticity [10]. Altogether, this supports the notion that features of macroscale brain activity originate from the dynamical properties of individual synapses.

If synaptic architecture modulates regional dynamics, how then does synaptic architecture influence a brain region's embedding and participation in global structural and functional networks? We find that SAP102 and PSD95 synapses make opposite contributions to global network topology. SAP102 synapses are present in regions that make many efferent structural connections, while PSD95 synapse density is correlated with functional hubs. Furthermore, the placement of structural

and functional hubs specifically reflects the presence of synapses that stably express PSD95 over the course of multiple days, weeks, or months [2]. These findings contribute to a growing body of literature that highlights the promise of enriching macroscale brain networks with microscale molecular information in revealing new insights about brain organization [25]. For example, previous work has reported that whole-brain network organization can be mapped to patterns of gene expression [41], protein abundance [38], cell type distributions [42, 43], and different types of oscillatory dynamics [44, 45]. Synapse architecture fills in the spaces between these other layers of description, thereby contributing to a more complete understanding of multiscale brain organization and the relationship between brain structure and function.

Why might some synapses express proteins with long lifetime while others express proteins with short lifetime? In general, protein turnover is an important process necessary for maintaining cellular health and tuning protein levels to a specific context [46, 47]. Indeed, protein turnover in synapses controls synaptic plasticity and may be a molecular marker of memory, such that synapses expressing long-lifetime proteins “hold on” to adaptations whereas synapses with short-lifetime proteins quickly reset [2, 48]. PSD95 lifetime in particular has been shown to be greatest in superficial layers of the isocortex (where longterm memories are stored [49]) and increases with age, presumably reflecting increased storage of long-term memory in late adulthood [50]. Meanwhile, short-lifetime PSD95 synapses are most expressed in the medulla, and during early development. The localization of long-lifetime PSD95 synapses in the isocortex and short-lifetime PSD95 synapses in the brainstem has led researchers to speculate that long-lifetime synaptic proteins are more involved in higher-order cognitive functions while short-lifetime synapses are related to innate behaviours [2]. However, we find that long-lifetime PSD95 synapses appear to play a similar role regardless of whether the mouse is awake or anaesthetized, whereas short-lifetime PSD95 synapses improve structure-function coupling specifically when mice are awake (Fig. 4). We therefore hypothesize that short-lifetime PSD95 synapses are involved in the moment-to-moment cognitive flexibility required during wakefulness, whereas long-lifetime PSD95 and SAP102 synapses support more fundamental functions related to homeostasis.

One promising future research direction in combining nanoscale synaptome mapping with macroscale whole-brain imaging is that of studying disease pathology. Synaptic pathology is a major cause of psychiatric, neurological, and developmental disorders affecting individuals across all ages [51]. Hundreds of genetic disorders target specific synaptic proteins and therefore specific synapse types [51, 52]. For example, both PSD95 and SAP102 synapses are targets of genetic disorders including childhood learning disabilities [53–56]. By map-

ping synapse types to brain dynamics and connectivity, we will develop a deeper understanding of how pathology in specific synapse types manifests throughout the brain. Ultimately, future studies combining synaptome mapping with brain imaging, in humans and model organisms, may enhance our understanding of how imaging can be used to monitor disease progression and therapeutic interventions.

We close with some methodological limitations. First, we only consider two excitatory synapse types. While PSD95 and SAP102 are both key synaptic proteins, the diversity of synapse types is only beginning to be fully appreciated and understood [1, 11, 57]. Extensive research is necessary to comprehensively characterize the spatial distribution, structure, and function of the many types of synapses that exist in the brain. Second, although whole-brain synapse mapping technology is both recent and state-of-the-art, current whole-brain synapse density maps are limited to a single male mouse, precluding an understanding of how synapse architecture varies across individuals. As synapse mapping technology becomes more high throughput, it will become possible to study how synaptic architecture influences individual-specific structure, function, and behaviour. Third, synapse density, tract-tracing and fMRI data were derived in separate mouse populations, highlighting the need for more comprehensive datasets that include measurements from diverse scales of brain organization.

In summary, we present synapse distribution as a novel molecular feature with direct influence on regional dynamics. As a result, the synaptic composition of a brain region will affect its participation in whole-brain structural and functional networks, as well as in different behavioural states. Altogether, this work illustrates the fundamental role of synapses in shaping whole-brain organization.

METHODS

All code and data used to conduct the analyses are available at https://github.com/netneurolab/hansen_synaptome.

Synapse mapping

Synapse density data was originally acquired and shared by Zhu et al. [1]. Briefly, the authors developed a novel synapse mapping pipeline (“SYNMAP”) to image and quantify multiple synaptic parameters for two synapse types: synapses that express the synaptic protein PSD95 (Postsynaptic Density 95) and those that express SAP102 (Synapse-Associated Protein 102). Both PSD95 and SAP102 are proteins postsynaptically expressed on excitatory neurons. They are members of the membrane-associated guanylate kinase (MAGUK) superfamily and function as scaffolding proteins which assemble neuro-

transmitter receptors, ion channels, and other structural and signaling proteins into a multiprotein signaling complex.

The authors use a single adult (postnatal day 80 male) genetically engineered mouse for whom its PSD95- and SAP102-coding genes (*Dlg4* and *Dlg3*) have been tagged with fluorescent proteins (eGFP and mKO2, respectively) such that the synaptic proteins are expressed alongside fluorescent proteins. All mouse procedures were performed in accordance with UK Home Office regulations and approved by Edinburgh University Director of Biological Services. The whole brain was dissected out and five $18\text{ }\mu\text{m}$ thick coronal slices were sectioned using a NX70 Termo Fisher cryostat. Fluorescently labelled proteins were imaged using a Spinning Disk confocal Microscopy (SDM) platform and quantified using an image detection algorithm, Ensemble Detection [1, 58, 59]. From here, synapses were classified as either expressing only PSD95, only SAP102, or both PSD95 and SAP102.

Next, six punctum parameters were quantified for each detected and localized synaptic puncta: mean punctum pixel intensity, punctum size, skewness, kurtosis, circularity, and aspect ratio (the latter four being measurements of punctum shape). Synaptic puncta parameters were averaged within each volumetric area ($19.2\text{ }\mu\text{m} \times 19.2\text{ }\mu\text{m} \times 0.5\text{ }\mu\text{m}$), then averaged over all volumetric areas within each of 775 anatomical regions defined by the Allen Reference Atlas (ARA) [60]. A weighted ensemble clustering (WEC) algorithm was applied to further cluster PSD95 and SAP102 synapses into 11 and 7 subtypes (and PSD95-SAP102 colocalized synapses into 19 subtypes), respectively, according to their synapse morphology. For each subtype, their density (number of detected and localized synaptic puncta per unit area) was mapped across the 775 regions of the ARA, resulting in a 37×775 matrix of synapse densities. In the present study, we analyze synapses that express only PSD95 or only SAP102 and do not analyze the colocalized synapse type, resulting in a 18×775 matrix of synapse densities (shown in Fig. 1a).

Rather than analyzing each subtype separately, we group subtypes according to how similarly they are anatomically expressed (Fig. 1b). We apply a consensus Louvain clustering algorithm ($\gamma = 1$, 250 repetitions [61, 62]) to the synapse similarity matrix and find two PSD95 clusters and one SAP102 cluster. Since SAP102 subtypes are all highly coexpressed, we average them together into a single mean SAP102 synapse density map (shown in Fig. 1g). PSD95 subtypes follow one of two expression patterns, which nearly perfectly divide PSD95 subtypes according to their PSD95 lifetime (save for one PSD95 subtype which has a short lifetime but is included in the “long-lifetime” cluster; Fig. 1b barplot). We therefore average PSD95 subtypes within each cluster into a long-lifetime PSD95 synapse density map (Fig. 1e) and a short-lifetime PSD95 synapse density map (Fig. 1f). Note that throughout, the labels “long-lifetime PSD95 synapses” and “short-lifetime

PSD95 synapses” refer to the lifetime of the protein (PSD95) and not the lifetime of the synaptic connection. Finally, for the analyses in the present report, the high spatial resolution synapse density data had to be downsampled. When applicable, synapse density was averaged across anatomical regions that fall within a single parent region, resulting in 88 bilateral regions when comparing with functional data, 137 right hemisphere regions when comparing with structural data, and 275 right hemisphere regions when comparing with gene expression data. For layer-specific analyses in Fig. 3c, 31 isocortical right hemisphere regions were available in layers I, V, VI, 30 were available in layer II/III, and 15 were available in layer IV. All mouse brains were plotted using *brainglobe-heatmap* (<https://github.com/brainglobe/brainglobe-heatmap>) [5].

Synapse protein lifetime quantification

Synapse protein lifetime data was collected by the same group that collected the synapse density data, as reported in Bulovaite et al. [2]. Briefly, the authors used HaloTag technology to measure PSD95 lifetime in PSD95-expressing synapses throughout the brain. HaloTag involves tagging PSD95 with a HaloTag domain, which then forms an irreversible bond with a HaloTag ligand, when the ligand is injected into the brain. By coupling the HaloTag ligand with a fluorophore, the authors are able to time the labelling of PSD95 synapses (according to when the injection of the HaloTag ligand occurs), then wait a defined amount of time before sacrificing the animal and imaging the synaptic puncta, using the methodology described in *Synapse mapping*. The number of synaptic puncta identified at time T is compared to the number of synaptic puncta identified immediately after injection, resulting in a measurement of the percentage of PSD95 synapses remaining after time T . In the present study, we use synapse protein lifetime data from 6 month-old female mice ($n = 8$ mice sacrificed day 0 after injection, and $n = 8$ mice sacrificed day 7 after injection). Synapse protein lifetime is defined as the percentage of PSD95 synapses remaining in the whole-brain at day 7 compared with day 0 (Figure 4a in [2]), and is quantified for each of the 11 PSD95 synapse subtypes.

Functional data acquisition

Resting-state fMRI scans were acquired by Gutierrez-Barragan et al. [4] in 10 awake, head-fixed C57BL/6J male mice (full methodological details available in [4]). First, a surgery was conducted to attach a custom-made headpost to the skull. This headpost was designed such that the mice could be secured to a custom-made MRI-compatible animal cradle which ensured immobilization during scanning. 10–15 days after the headpost surgery, the mice followed a habituation protocol to become accli-

matized to the scanning procedure. The habituation protocol involved multiple days of habituation to the experimenter, the cradle, head fixation, scanning environment, and scanning sounds. All fMRI scans were acquired on a 7.0 Tesla MRI scanner (Bruker Biospin, Ettlingen) with a BGA-9 gradient set, a 72 mm birdcage transmit coil, and a four-channel solenoid receive coil. A single-shot echo planar imaging (EPI) sequence was acquired with the following parameters: TR/TE=1000/15ms, flip angle=60°, matrix=100 × 100, FOV=2.3×2.3 cm, 18 coronal slices (voxel-size: 230×230×600 μ m), slice thickness=600 μ m, and 1920 time points (32 minutes total).

BOLD data preprocessing involved removing the first 2 minutes of every time-series, time despiking, motion correction, skull stripping, and spatial registration to an in-house mouse brain template with spatial resolution of 0.23 × 0.23 × 0.6 mm³ [63]. Denoising and motion correction involved regressing out average cerebral spinal fluid signal, as well as 24 motion parameters determined from the 3 translation and rotation parameters estimated during motion correction, their temporal derivatives, and corresponding squared regressors. No global signal regression was performed. Frame-wise displacement (FD)-derived measurements of in-scanner head motion were not significantly different as those obtained in anaesthetized animals. Furthermore, frame-wise fMRI scrubbing was employed, using an FD threshold of 0.075 mm. Finally, the time-series were band-pass filtered (0.01 – 0.1 Hz) and spatially smoothed with a Gaussian kernel of 0.5 mm full width at half maximum.

Two additional groups of age matched male C57BL/6J mice were scanned under anaesthesia in Gutierrez-Barragan et al. [4]. The first group includes 19 mice scanned under shallow halothane anaesthesia (0.75%) [64]. The second group includes 14 mice scanned under medetomidine-isoflurane anaesthesia (0.05 mg/kg bolus and 0.1 mg/kg/h IV infusion, plus 0.5% isoflurane). All imaged mice, awake and anesthetized, were imaged in the same lab, bred in the same vivarium, and scanned with the same MRI protocol.

Finally, fMRI volumes for each mouse was parcellated to 162 regions defined by the ARA, of which only 88 regions were also present in the synapse density data. Due to motion scrubbing, different mice had a different number of time-points, with the minimum being 1414; therefore, time-series for the remaining mice were all truncated from the end to 1414 time-points. The final fMRI data for all mice had size 88 regions × 1414 time-points.

Time-series feature extraction

For every mouse and every brain region, the corresponding time-series was subjected to an automated massive time-series feature extraction pipeline using the Highly Comparative Time-Series Analysis toolbox (*hctsa*, <https://github.com/benfulcher/hctsa> [20, 21]). This toolbox calculates > 7 000 statistical features (e.g. mean, vari-

ance, stationarity, entropy) on each time-series and normalizes the features across brain regions to the unit interval using a scaled robust sigmoid normalization (parameter *normFunction*= ‘mixedSigmoid’). After discarding features with zero variance across regions, we retained the subset of features present across all mice, then averaged feature values across mice, resulting in a 88 region × 6 471 feature matrix of time-series feature values (shown in Fig. 2c).

We next correlate each time-series feature with synapse density. After Bonferroni multiple comparisons correction, we find 26 features are significantly correlated with long-lifetime PSD95 synapse density, 6 features are significantly correlated with short-lifetime synapse density, and 211 features are significantly correlated with SAP102 synapse density (see Supplementary Table S1 for feature names, correlation coefficient, and corrected *p*-value). Due to the small number of features that are correlated with short-lifetime PSD95 synapses, as well as their relatively small correlation coefficient (all with magnitude < 0.5) and large *p*-value (none < 0.01), we do not further analyze features associated with short-lifetime PSD95 synapses.

For the other two synapse types, we calculate a feature × feature similarity matrix for significantly correlated features (in the case of SAP102, we also threshold these features to those where *r* > 0.5, to reduce the set from 211 features to 59). This similarity matrix was clustered into 2–10 clusters using agglomerative clustering and we show one clustering solution in Fig. S2a (long-lifetime PSD95) and Fig. S3a (SAP102). We triangulate toward a single representative feature to highlight in the main text by considering (1) correlation coefficient magnitude, (2) number of features that measure a similar property, which can be estimated via cluster size, and (3) feature explainability.

For long-lifetime PSD95 synapses, we selected StatAv10 [22], which is calculated by binning the time-series into ten non-overlapping segments, calculating the mean of each segment, calculating the standard deviation across the ten segment means, and normalizing this standard deviation with the standard deviation of the full time-series (Fig. S2b). For SAP102 synapses, we selected DN_OutlierInclude_n_001_mrmrd which, for all “extreme” events below a moving threshold (in this case, thresholds are all ≤ 0), calculates the mean time at which all below-threshold events occur (time being normalized such that -1 is the start of the time-series, 0 is the middle, and 1 is the final time point), then calculates the median mean time across all thresholds (Fig. S3b).

Structural data acquisition

The Allen Mouse Brain Connectivity Atlas was first presented in Oh et al. [3] and maps axonal projections for 295 ARA-defined brain regions in C57BL/6J male mice at postnatal age P56. Each mouse brain was sectioned into

140 slices ($0.35\text{ }\mu\text{m }x\text{-}y$ resolution, $100\text{ }\mu\text{m}$ thickness), and a eGFP-labelled anterograde tracer was injected into multiple anatomical regions on each slice. Each slice was registered to the Allen Reference Atlas at a resolution of $100\text{ }\mu\text{m}^3$. In total, 469 viral microinjection experiments were conducted to map axonal connectivity.

Next, Oh et al. [3] summarized the connectivity data in a weighted, directed adjacency matrix with includes a normalized connection strength and an associated p -value for ipsilateral connections in the right hemisphere and contralateral connections from right to left hemisphere (Supplementary Table 2 of [3]). 80 brain regions were excluded due to insufficiently labelled voxels from the injection experiment, and an additional 2 regions were excluded because they were not linearly separable under the connectivity model given the full dataset, resulting in a final connectivity matrix representing 213 source regions, 213 ipsilateral target regions, and 213 contralateral target regions.

In the present report, we focus solely on ipsilateral connectivity in the right hemisphere (213×213 weighted directed adjacency matrix). As per Fulcher and Fornito [65], we omit connections where $p < 0.05$ (excluding self-connections), resulting in a connection density of 6.9%. Finally, we reduced the set of regions to those also present in the synapse density data, resulting in a 137×137 weighted and directed structural connectivity matrix.

Structure-function coupling

Structure-function coupling at every brain region is defined as the adjusted R^2 of a simple linear regression model that fits regional communicability (i.e. the communicability between a brain region to every other brain region) to regional functional connectivity (i.e. the functional connectivity between a brain region and every other brain region). Communicability is defined as the weighted average of all walks and paths between two brain regions, as defined on the structural connectivity matrix, and represents diffusive communication [66, 67]. Additionally, communicability has been previously demonstrated as an important bridge between brain structure and function [26, 27, 38, 68]. In the synapse-informed model, regional synapse type density for long-lifetime PSD95, short-lifetime PSD95, and SAP102 synapses separately, is included as an independent variable. The change in fit (ΔR_{adj}^2) is defined as the difference between R_{adj}^2 before and after adding synapse type density to the model. The distribution of ΔR_{adj}^2 for all regions was compared across states (awake versus anaesthetized) using a two-sided dependent non-parametric t-test for paired samples (Wilcoxon signed-rank test). To conduct this analysis, we used the subset of brain regions present in the structural, functional, and synapse density datasets, resulting in 35 right hemi-

sphere brain regions.

Gene expression data acquisition

In situ hybridization data were obtained from the Allen Mouse Brain Atlas for adult C57BL/6J male mice (age P56) [23]. Using the abagen toolbox (<https://abagen.readthedocs.io/en/stable/> [69]), gene expression density data (proportion of expressed voxels in an anatomical division) was downloaded for the 275 unique Allen Reference Atlas regions for which synapse density data are also defined. Data were averaged across experiments, and were separately downloaded for data from sagittal (19919 genes) and coronal (4083 genes) brain sections. Gene expression was normalized using a robust sigmoid transformation [20, 65], such that

$$x_{\text{norm}} = \frac{1}{1 + \exp(-\frac{(x - \langle x \rangle)}{\text{IQR}_x})}$$

where x_{norm} is the normalized expression value of the gene, $\langle x \rangle$ is the median and IQR_x is the normalized interquartile range of gene expression across regional samples. Normalized expression values were then rescaled to the unit interval:

$$x_{\text{scaled}} = \frac{x_{\text{norm}} - \min(x_{\text{norm}})}{\max(x_{\text{norm}}) - \min(x_{\text{norm}})}$$

For univariate correlations between gene expression and synapse density, we only consider genes whose expression is (1) measured in both sagittal and coronal sections, and (2) the correlation of gene expression from sagittal and coronal sections is ≥ 0.70 , resulting in a total of 1295 genes. The correlational analysis uses gene expression measurements from coronal sections. For the gene ontology analysis in Fig. 5c–d, we use the full set of genes acquired using sagittal sections.

Gene ontology analysis

To understand the function of genes that are coexpressed with specific synapse types, we conduct a gene category enrichment analysis. We use Gene Ontology biological processes and annotations, downloaded from <https://zenodo.org/records/4460714> [70] (see also <https://github.com/benfulcher/GeneCategoryEnrichmentAnalysis> [71]), which were originally downloaded directly from <https://geneontology.org/docs/go-enrichment-analysis/> [72]. This database includes 30 248 biological processes, each associated with a list of genes. We calculate a “category score” for each biological process, defined as the median absolute Spearman’s correlation between a gene’s expression and synapse density, across all genes

in the category. We only consider categories with at least 100 associated genes, resulting in 1 616 categories.

Cell type density

Density (mm^3) of cells (all), neurons, glia, excitatory cells, inhibitory cells, modulatory cells, astrocytes, oligodendrocytes, and microglia in the mouse brain are derived from Nissl microscopy data in the Allen Mouse Brain Atlas [23] and can be found in supplementary data sheet 2 of Erö et al. [73]. Since region names in the cell density dataset do not include hemisphere, we compare the brain regions in the cell density atlas with the 44 name-matched left hemisphere regions from the functional parcellation (Fig. 1d). Correlations are shown in Fig. S9.

Acknowledgments

BM acknowledges support from the Natural Sciences and Engineering Research Council of Canada (NSERC), Canadian Institutes of Health Research (CIHR), Brain Canada Foundation Future Leaders Fund, the Canada Research Chairs Program, the Michael J. Fox Foundation, and the Healthy Brains for Healthy Lives initiative. JYH acknowledges support from the Helmholtz International BigBrain Analytics & Learning Laboratory and the Natural Sciences and Engineering Research Council of Canada. AG acknowledges support by the European Research Council (ERC-DISCONN No. 802371, BRAINAMICS No. 101125054) and Sara and Paolo Baracchino. The funders had no role in study design, data collection and analysis, decision to publish or preparation of the manuscript.

-
- [1] Fei Zhu, Mélissa Cizeron, Zhen Qiu, Ruth Benavides-Piccione, Maksym V Kopanitsa, Nathan G Skene, Babis Koniaris, Javier DeFelipe, Erik Fransen, Noboru H Komiyama, et al. Architecture of the mouse brain synaptome. *Neuron*, 99(4):781–799, 2018.
 - [2] Edita Bulovaite, Zhen Qiu, Maximilian Kratschke, Adrianna Zgraj, David G Fricker, Eleanor J Tuck, Ragini Gokhale, Babis Koniaris, Shekib A Jami, Paula Merino-Serrais, et al. A brain atlas of synapse protein lifetime across the mouse lifespan. *Neuron*, 110(24):4057–4073, 2022.
 - [3] Seung Wook Oh, Julie A Harris, Lydia Ng, Brent Winslow, Nicholas Cain, Stefan Mihalas, Quanxin Wang, Chris Lau, Leonard Kuan, Alex M Henry, et al. A mesoscale connectome of the mouse brain. *Nature*, 508(7495):207–214, 2014.
 - [4] Daniel Gutierrez-Barragan, Neha Atulkumar Singh, Filomena Grazia Alvino, Ludovico Coletta, Federico Rocchi, Elizabeth De Guzman, Alberto Galbusera, Mauro Ubaldi, Stefano Panzeri, and Alessandro Gozzi. Unique spatiotemporal fmri dynamics in the awake mouse brain. *Current biology*, 32(3):631–644, 2022.
 - [5] Federico Claudi, Adam Tyson, Luigi Petrucco, Mathieu Bourdenx, carlocastoldi, Rami Hamati, and Alessandro Felder. brainglobe/brainglobe-heatmap. Zenodo, <https://doi.org/10.5281/zenodo.10375287>, 2024.
 - [6] Seth GN Grant. Toward a molecular catalogue of synapses. *Brain research reviews*, 55(2):445–449, 2007.
 - [7] Nancy A O’ourke, Nicholas C Weiler, Kristina D Micheva, and Stephen J Smith. Deep molecular diversity of mammalian synapses: why it matters and how to measure it. *Nature Reviews Neuroscience*, 13(6):365–379, 2012.
 - [8] Martine Migaud, Paul Charlesworth, Maureen Dempster, Lorna C Webster, Ayako M Watabe, Michael Makhinson, Yong He, Mark F Ramsay, Richard GM Morris, John H Morrison, et al. Enhanced long-term potentiation and impaired learning in mice with mutant postsynaptic density-95 protein. *Nature*, 396(6710):433–439, 1998.
 - [9] Holly J Carlisle, Ann E Fink, Seth GN Grant, and Thomas J O’Dell. Opposing effects of psd-93 and psd-95 on long-term potentiation and spike timing-dependent plasticity. *The Journal of physiology*, 586(24):5885–5900, 2008.
 - [10] Peter C Cuthbert, Lianne E Stanford, Marcelo P Coba, James A Ainge, Ann E Fink, Patricio Opazo, Jary Y Delgado, Noboru H Komiyama, Thomas J O’Dell, and Seth GN Grant. Synapse-associated protein 102/dlg3 couples the nmda receptor to specific plasticity pathways and learning strategies. *Journal of Neuroscience*, 27(10):2673–2682, 2007.
 - [11] Mélissa Cizeron, Zhen Qiu, Babis Koniaris, Ragini Gokhale, Noboru H Komiyama, Erik Fransén, and Seth GN Grant. A brainwide atlas of synapses across the mouse life span. *Science*, 369(6501):270–275, 2020.
 - [12] Jess Nithianantharajah, Noboru H Komiyama, Andrew McKechnie, Mandy Johnstone, Douglas H Blackwood, David St Clair, Richard D Emes, Louie N Van De Lagemaat, Lisa M Saksida, Timothy J Bussey, et al. Synaptic scaffold evolution generated components of vertebrate cognitive complexity. *Nature neuroscience*, 16(1):16–24, 2013.
 - [13] Evelyn MR Lake, Xinxin Ge, Xilin Shen, Peter Herman, Fahmeed Hyder, Jessica A Cardin, Michael J Higley, Dustin Scheinost, Xenophon Papademetris, Michael C Crair, et al. Simultaneous cortex-wide fluorescence ca²⁺ imaging and whole-brain fmri. *Nature methods*, 17(12):1262–1271, 2020.
 - [14] Alessandro Gozzi and Adam J Schwarz. Large-scale functional connectivity networks in the rodent brain. *Neuroimage*, 127:496–509, 2016.
 - [15] Francesco Sforazzini, Adam J Schwarz, Alberto Galbusera, Angelo Bifone, and Alessandro Gozzi. Distributed bold and cbv-weighted resting-state networks in the mouse brain. *Neuroimage*, 87:403–415, 2014.
 - [16] Valerio Zerbi, Joanes Grandjean, Markus Rudin, and Nicole Wenderoth. Mapping the mouse brain with rs-fmri: An optimized pipeline for functional network identification. *Neuroimage*, 123:11–21, 2015.
 - [17] Hadi Vafaii, Francesca Mandino, Gabriel Desrosiers-Grégoire, David O’Connor, Marija Markicevic, Xilin Shen, Xinxin Ge, Peter Herman, Fahmeed Hyder, Xenophon Papademetris, et al. Multimodal measures of spontaneous brain activity reveal both common and divergent patterns of cortical functional organization. *Nature Communications*

- tions, 15(1):229, 2024.
- [18] Sarab S Sethi, Valerio Zerbi, Nicole Wenderoth, Alex Fornito, and Ben D Fulcher. Structural connectome topology relates to regional bold signal dynamics in the mouse brain. *Chaos: An Interdisciplinary Journal of Nonlinear Science*, 27(4), 2017.
- [19] Joanes Grandjean, Aileen Schroeter, Imene Batata, and Markus Rudin. Optimization of anesthesia protocol for resting-state fmri in mice based on differential effects of anesthetics on functional connectivity patterns. *Neuroimage*, 102:838–847, 2014.
- [20] Ben D Fulcher, Max A Little, and Nick S Jones. Highly comparative time-series analysis: the empirical structure of time series and their methods. *Journal of the Royal Society Interface*, 10(83):20130048, 2013.
- [21] Ben D Fulcher and Nick S Jones. hcts: A computational framework for automated time-series phenotyping using massive feature extraction. *Cell systems*, 5(5):527–531, 2017.
- [22] Steven M Pincus, Theodore R Cummins, and Gabriel G Haddad. Heart rate control in normal and aborted-sids infants. *American Journal of Physiology-Regulatory, Integrative and Comparative Physiology*, 264(3):R638–R646, 1993.
- [23] Ed S Lein, Michael J Hawrylycz, Nancy Ao, Mikael Ayres, Amy Bensinger, Amy Bernard, Andrew F Boe, Mark S Boguski, Kevin S Brockway, Emi J Byrnes, et al. Genome-wide atlas of gene expression in the adult mouse brain. *Nature*, 445(7124):168–176, 2007.
- [24] Laura E Suárez, Ross D Markello, Richard F Betzel, and Bratislav Misic. Linking structure and function in macroscale brain networks. *Trends in cognitive sciences*, 24(4):302–315, 2020.
- [25] Vincent Bazinet, Justine Y Hansen, and Bratislav Misic. Towards a biologically annotated brain connectome. *Nature reviews neuroscience*, 24(12):747–760, 2023.
- [26] Bertha Vázquez-Rodríguez, Laura E Suárez, Ross D Markello, Golia Shafiei, Casey Paquola, Patric Hagmann, Martijn P Van Den Heuvel, Boris C Bernhardt, R Nathan Spreng, and Bratislav Misic. Gradients of structure-function tethering across neocortex. *Proceedings of the National Academy of Sciences*, 116(42):21219–21227, 2019.
- [27] Graham L Baum, Zaixu Cui, David R Roalf, Rastko Ceric, Richard F Betzel, Bart Larsen, Matthew Cieslak, Philip A Cook, Cedric H Xia, Tyler M Moore, et al. Development of structure–function coupling in human brain networks during youth. *Proceedings of the National Academy of Sciences*, 117(1):771–778, 2020.
- [28] Zhen-Qi Liu, Bertha Vazquez-Rodriguez, R Nathan Spreng, Boris C Bernhardt, Richard F Betzel, and Bratislav Misic. Time-resolved structure–function coupling in brain networks. *Communications biology*, 5(1):532, 2022.
- [29] Farnaz Zamani Esfahlani, Joshua Faskowitz, Jonah Slack, Bratislav Mišić, and Richard F Betzel. Local structure–function relationships in human brain networks across the lifespan. *Nature communications*, 13(1):2053, 2022.
- [30] Mark O Collins, Holger Husi, Lu Yu, Julia M Brandon, Chris NG Anderson, Walter P Blackstock, Jyoti S Choudhary, and Seth GN Grant. Molecular characterization and comparison of the components and multiprotein complexes in the postsynaptic proteome. *Journal of neurochemistry*, 97:16–23, 2006.
- [31] Stephen N Gomperts. Clustering membrane proteins: It's all coming together with the psd-95/sap90 protein family. *Cell*, 84(5):659–662, 1996.
- [32] Ayse Dosemeci, Anthony J Makusky, Ewa Jankowska-Stephens, Xiaoyu Yang, Douglas J Slotta, and Sanford P Markey. Composition of the synaptic psd-95 complex. *Molecular & Cellular Proteomics*, 6(10):1749–1760, 2007.
- [33] Andreas K Engel, Pascal Fries, and Wolf Singer. Dynamic predictions: oscillations and synchrony in top–down processing. *Nature Reviews Neuroscience*, 2(10):704–716, 2001.
- [34] Xiao-Jing Wang. Macroscopic gradients of synaptic excitation and inhibition in the neocortex. *Nature reviews neuroscience*, 21(3):169–178, 2020.
- [35] Gyorgy Buzsaki and Andreas Draguhn. Neuronal oscillations in cortical networks. *science*, 304(5679):1926–1929, 2004.
- [36] György Buzsáki, Costas A Anastassiou, and Christof Koch. The origin of extracellular fields and currents—eeg, ecog, lfp and spikes. *Nature reviews neuroscience*, 13(6):407–420, 2012.
- [37] Shreejoy J Tripathy, Lilah Toker, Brenna Li, Cindy-Lee Crichlow, Dmitry Tebaykin, B Ogan Mancarci, and Paul Pavlidis. Transcriptomic correlates of neuron electrophysiological diversity. *PLoS computational biology*, 13(10):e1005814, 2017.
- [38] Justine Y Hansen, Golia Shafiei, Ross D Markello, Kelly Smart, Sylvia ML Cox, Martin Nørgaard, Vincent Beliveau, Yanjun Wu, Jean-Dominique Gallezot, Étienne Aumont, et al. Mapping neurotransmitter systems to the structural and functional organization of the human neocortex. *Nature neuroscience*, 25(11):1569–1581, 2022.
- [39] Golia Shafiei, Ben D Fulcher, Bradley Voytek, Theodore D Satterthwaite, Sylvain Baillet, and Bratislav Misic. Neurophysiological signatures of cortical micro-architecture. *Nature communications*, 14(1):6000, 2023.
- [40] Golia Shafiei, Ross D Markello, Reinder Vos de Wael, Boris C Bernhardt, Ben D Fulcher, and Bratislav Misic. Topographic gradients of intrinsic dynamics across neocortex. *elife*, 9:e62116, 2020.
- [41] Alex Fornito, Aurina Arnatkeviciute, and Ben D Fulcher. Bridging the gap between connectome and transcriptome. *Trends Cogn Sci*, 23(1):34–50, 2019.
- [42] Casey Paquola, Reinder Vos De Wael, Konrad Wagstyl, Richard AI Bethlehem, Seok-Jun Hong, Jakob Seidlitz, Edward T Bullmore, Alan C Evans, Bratislav Misic, Daniel S Margulies, et al. Microstructural and functional gradients are increasingly dissociated in transmodal cortices. *PLoS biology*, 17(5):e3000284, 2019.
- [43] Yongbin Wei, Lianne H Scholtens, Elise Turk, and Martijn P Van Den Heuvel. Multiscale examination of cytoarchitectonic similarity and human brain connectivity. *Network Neuroscience*, 3(1):124–137, 2018.
- [44] Sharna D Jamadar, Phillip GD Ward, Emma X Liang, Edwina R Orchard, Zhaolin Chen, and Gary F Egan. Metabolic and hemodynamic resting-state connectivity of the human brain: a high-temporal resolution simultaneous bold-fMRI and fDG-fPET multimodality study. *Cerebral Cortex*, 31(6):2855–2867, 2021.
- [45] Matthew J Brookes, Joanne R Hale, Johanna M Zumer, Claire M Stevenson, Susan T Francis, Gareth R Barnes, Julia P Owen, Peter G Morris, and Srikantan S Nagarajan. Measuring functional connectivity using meg: methodology and comparison with fMRI. *Neuroimage*, 56(3):1082–1104, 2011.

- [46] Susmita Kaushik and Ana Maria Cuervo. Proteostasis and aging. *Nature medicine*, 21(12):1406–1415, 2015.
- [47] William E Balch, Richard I Morimoto, Andrew Dillin, and Jeffery W Kelly. Adapting proteostasis for disease intervention. *science*, 319(5865):916–919, 2008.
- [48] Francis Crick. Neurobiology: memory and molecular turnover. *Nature*, 312(5990):101–101, 1984.
- [49] Larry R Squire and Adam JO Dede. Conscious and unconscious memory systems. *Cold Spring Harbor perspectives in biology*, 7(3):a021667, 2015.
- [50] Elliot M Tucker-Drob. Differentiation of cognitive abilities across the life span. *Developmental psychology*, 45(4):1097, 2009.
- [51] Àlex Bayés, Louie N Van De Lagemaat, Mark O Collins, Mike DR Croning, Ian R Whittle, Jyoti S Choudhary, and Seth GN Grant. Characterization of the proteome, diseases and evolution of the human postsynaptic density. *Nature neuroscience*, 14(1):19–21, 2011.
- [52] Seth GN Grant. Synapse diversity and synaptome architecture in human genetic disorders. *Human Molecular Genetics*, 28(R2):R219–R225, 2019.
- [53] Agustí Rodríguez-Palmero, Melissa María Boerrigter, David Gómez-Andrés, Kimberly A Aldinger, Íñigo Marcos-Alcalde, Bernt Popp, David B Everman, Alycia Kern Lovgren, Stephanie Arpin, Vahid Bahrambeigi, et al. Dlg4-related synaptopathy: a new rare brain disorder. *Genetics in Medicine*, 23(5):888–899, 2021.
- [54] Sachi Tokunaga, Hideki Shimomura, Naoko Taniguchi, Kumiko Yanagi, Tadashi Kaname, Nobuhiko Okamoto, and Yasuhiro Takeshima. A novel dlg4 variant causes dlg4-related synaptopathy with intellectual regression. *Human Genome Variation*, 11(1):1, 2024.
- [55] Patrick Tarpey, Josep Parnau, Matthew Blow, Hayley Woffendin, Graham Bignell, Charles Cox, James Cox, Helen Davies, Sarah Edkins, Simon Holden, et al. Mutations in the dlg3 gene cause nonsyndromic x-linked mental retardation. *The American Journal of Human Genetics*, 75(2):318–324, 2004.
- [56] Anna Sandestig, Anna Green, Johan Aronsson, Katarina Ellnebo, and Margarita Stefanova. A novel dlg3 mutation expanding the phenotype of x-linked intellectual disability caused by dlg3 nonsense variants. *Molecular Syndromology*, 10(5):281–285, 2019.
- [57] Richard D Emes and Seth GN Grant. Evolution of synapse complexity and diversity. *Annual review of neuroscience*, 35(1):111–131, 2012.
- [58] Zhen Qiu, Lei Yang, and Weiping Lu. A new feature-preserving nonlinear anisotropic diffusion for denoising images containing blobs and ridges. *Pattern Recognition Letters*, 33(3):319–330, 2012.
- [59] Zhi-Hua Zhou. *Ensemble methods: foundations and algorithms*. CRC press, 2012.
- [60] Hong Wei Dong. *The Allen reference atlas: A digital color brain atlas of the C57BL/6J male mouse*. John Wiley & Sons Inc, 2008.
- [61] Vincent D Blondel, Jean-Loup Guillaume, Renaud Lambiotte, and Etienne Lefebvre. Fast unfolding of communities in large networks. *Journal of statistical mechanics: theory and experiment*, 2008(10):P10008, 2008.
- [62] Danielle S Bassett, Mason A Porter, Nicholas F Wymbs, Scott T Grafton, Jean M Carlson, and Peter J Mucha. Robust detection of dynamic community structure in networks. *Chaos: An Interdisciplinary Journal of Nonlinear Science*, 23(1):013142, 2013.
- [63] Federico Rocchi, Carola Canella, Shahryar Noei, Daniel Gutierrez-Barragan, Ludovico Coletta, Alberto Galbusera, Alexia Stuefer, Stefano Vassanelli, Massimo Pasqualetti, Giuliano Iurilli, et al. Increased fmri connectivity upon chemogenetic inhibition of the mouse prefrontal cortex. *Nature communications*, 13(1):1056, 2022.
- [64] Daniel Gutierrez-Barragan, M Albert Basson, Stefano Panzeri, and Alessandro Gozzi. Infraslow state fluctuations govern spontaneous fmri network dynamics. *Current Biology*, 29(14):2295–2306, 2019.
- [65] Ben D Fulcher and Alex Fornito. A transcriptional signature of hub connectivity in the mouse connectome. *Proceedings of the National Academy of Sciences*, 113(5):1435–1440, 2016.
- [66] Ernesto Estrada, Desmond J Higham, and Naomichi Hatano. Communicability and multipartite structures in complex networks at negative absolute temperatures. *Physical Review E—Statistical, Nonlinear, and Soft Matter Physics*, 78(2):026102, 2008.
- [67] Jonathan J Crofts and Desmond J Higham. A weighted communicability measure applied to complex brain networks. *Journal of the Royal Society Interface*, 6(33):411–414, 2009.
- [68] Caio Seguin, Olaf Sporns, Andrew Zalesky, Fernando Calamante, et al. Network communication models narrow the gap between the modular organization of structural and functional brain networks. *NeuroImage*, 257:119323, 2022.
- [69] Ross D Markello, Aurina Arnatkeviciute, Jean-Baptiste Poline, Ben D Fulcher, Alex Fornito, and Bratislav Misic. Standardizing workflows in imaging transcriptomics with the abagen toolbox. *elife*, 10:e72129, 2021.
- [70] Ben D Fulcher. Raw and processed go term data to support running gcea analyses using ensemble-based nulls, as described in the manuscript, 'overcoming bias in gene category enrichment analyses of brain-wide transcriptomic data'. *Zenodo*, doi.org/10.5281/zenodo.4460714, 2021.
- [71] Ben D Fulcher, Aurina Arnatkeviciute, and Alex Fornito. Overcoming false-positive gene-category enrichment in the analysis of spatially resolved transcriptomic brain atlases data. *Nature communications*, 12(1):2669, 2021.
- [72] Michael Ashburner, Catherine A Ball, Judith A Blake, David Botstein, Heather Butler, J Michael Cherry, Allan P Davis, Kara Dolinski, Selina S Dwight, Janan T Eppig, et al. Gene ontology: tool for the unification of biology. *Nature genetics*, 25(1):25–29, 2000.
- [73] Csaba Erő, Marc-Oliver Gewaltig, Daniel Keller, and Henry Markram. A cell atlas for the mouse brain. *Frontiers in neuroinformatics*, 12:84, 2018.

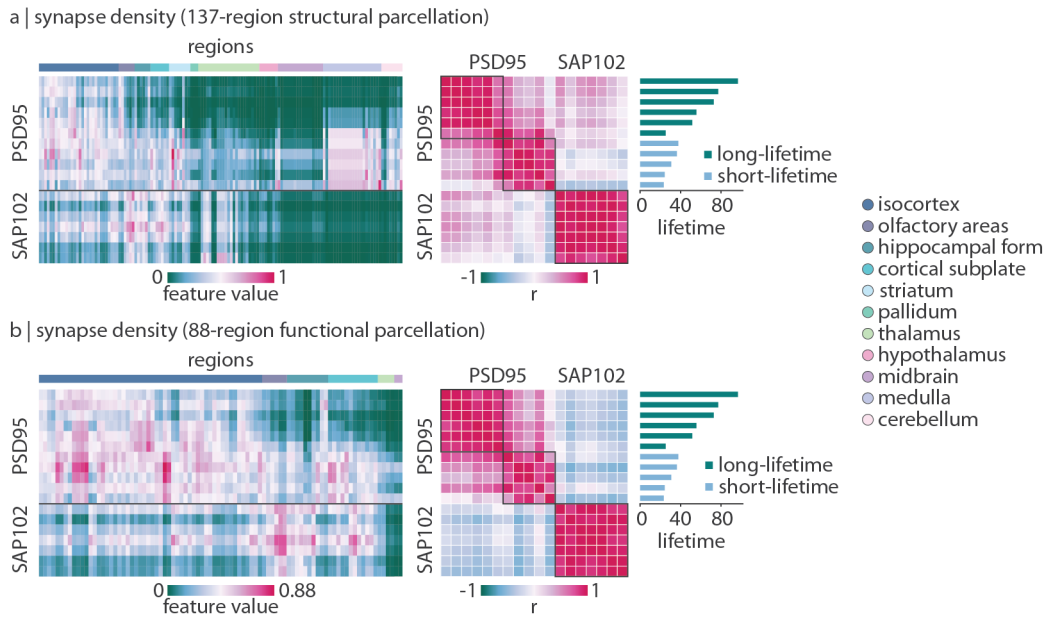
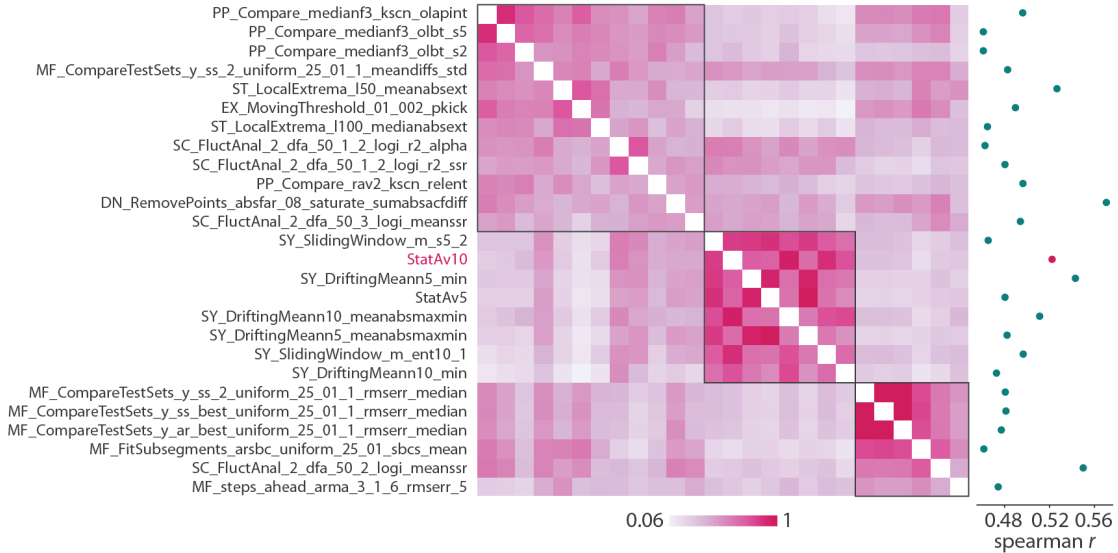


Figure S1. Parcellated synapse type density in the mouse brain | We repeat what is shown in Fig. 1a–b, parcellated to (a) the 137-region right hemisphere parcellation and (b) the 88-region bilateral parcellation. Regions in the lefthand synapse density matrix are ordered by ontological structure, as indicated by the colours in the horizontal bar. The righthand similarity matrix represents how similarly (Spearman's r) pairs of synapse subtypes are spatially expressed. Clusters are derived using the Louvain community detection algorithm [61, 62].

a | time-series features most correlated with long-lifetime PSD95 synapse density



b | StatAv10 in two example time-series

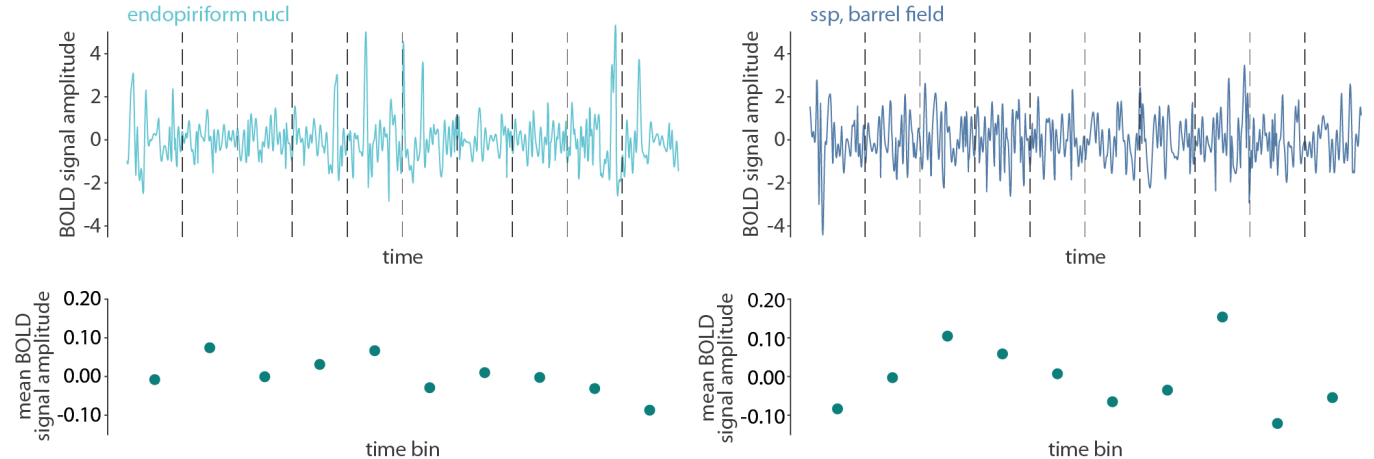


Figure S2. Time-series features most associated with long-lifetime PSD95 synapse density | We correlate long-lifetime PSD95 synapse density with each of 6 471 time-series features. (a) We generate a feature \times feature correlation matrix (Spearman r) for the 26 time-series features that are significantly correlated with long-lifetime PSD95 synapse density after Bonferroni correction. The correlation between each time-series feature and long-lifetime PSD95 synapse density is shown in the scatter plot on the right of the matrix. One feature (StatAv10 [22]) is selected as a representative feature in the main text. (b) StatAv10 is calculated by dividing a z-scored time-series into ten non-overlapping bins (dashed vertical lines), calculating the mean signal amplitude within each bin, normalized by the standard deviation of the full time-series (green points), then calculating the standard deviation across normalized bin means. We illustrate this process for two example time-series, one (endopiriform nucleus) with low long-lifetime PSD95 synapse density (and low StatAv10), and the other (primary somatosensory area, barrel field) with large long-lifetime PSD95 synapse density (and high StatAv10).

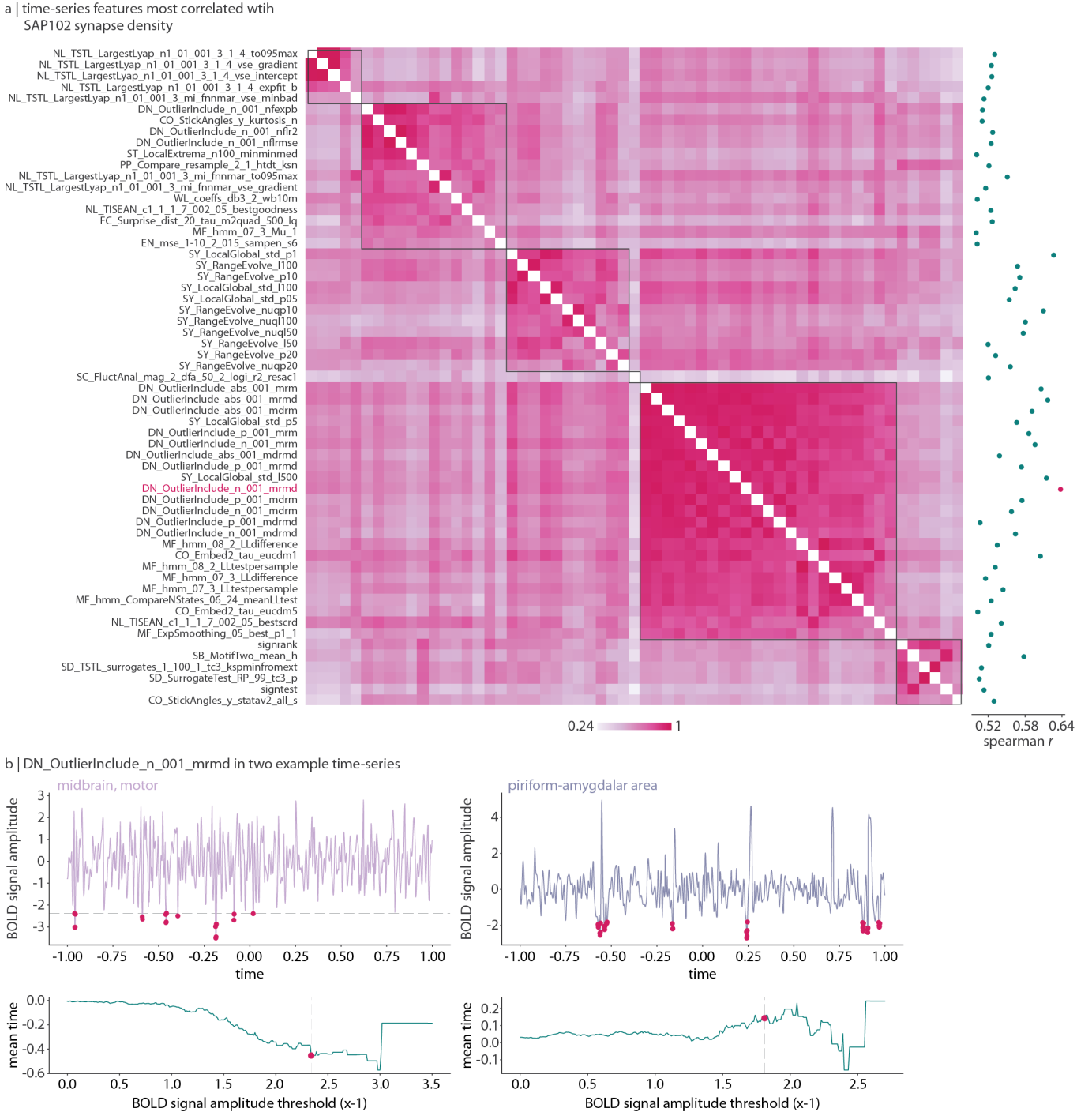


Figure S3. Time-series features most associated with SAP102 synapse density | We correlate SAP102 synapse density with each of 6 471 time-series features. (a) We generate a feature \times feature correlation matrix (Spearman r) for the 59 time-series features that are both significantly correlated with SAP102 synapse density and $r > 0.5$. The correlation between each time-series feature and SAP102 synapse density is shown in the scatter plot on the right of the matrix. One feature (DN_OutlierInclude_n_001_mrrmd) is selected as a representative feature in the main text. (b) DN_OutlierInclude_n_001_mrrmd is calculated by defining a threshold from 0 to -3.5 (0.01 increments; x -axis of the green plot; example threshold shown as the horizontal dashed line in the time-series plots at the top and as a vertical dashed line in the green plots at the bottom), selecting all time-points where the z-scored time-series' value is below the threshold (pink points on the time-series; time is normalized from -1 to 1), calculating the mean time at which these extreme events occur (y -axis of the green plot), and finally calculating the median mean time across all thresholds. We illustrate this process for two example time-series, one (midbrain, motor area) with low SAP102 synapse density (and a lower DN_OutlierInclude_n_001_mrrmd, that is, an earlier occurrence of extreme events) and one (piriform-amygdalar area) with high SAP102 synapse density (and a higher DN_OutlierInclude_n_001_mrrmd, that is, a later occurrence of extreme events).

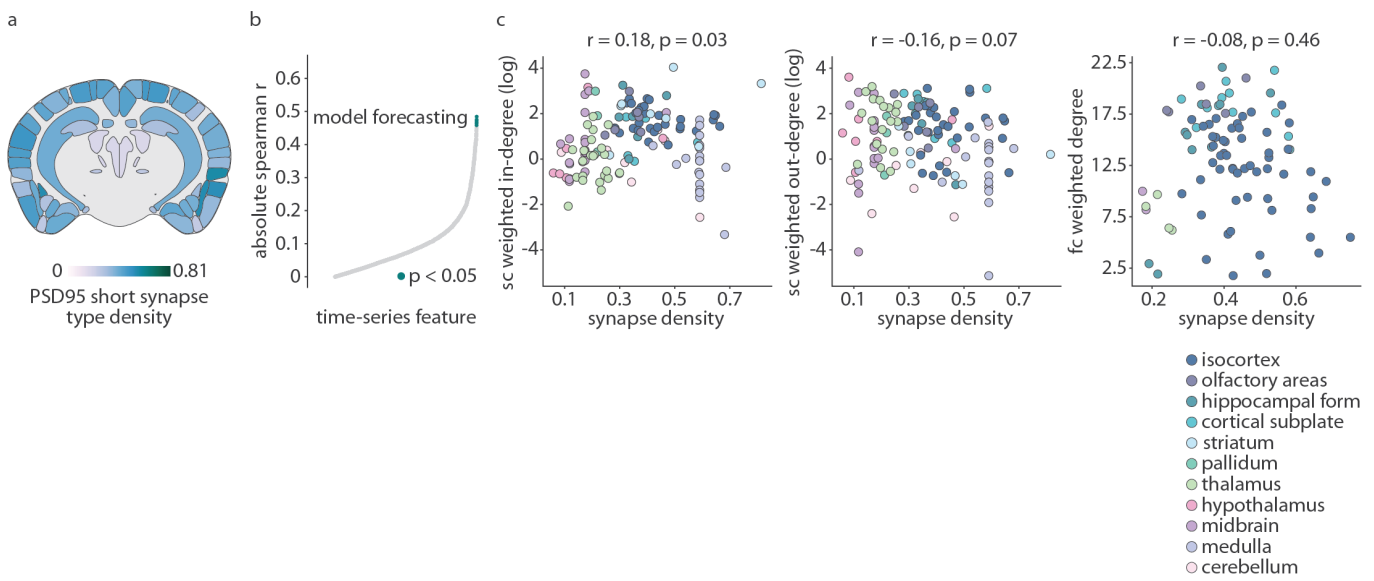


Figure S4. Time-series and interregional connectivity profiling of short-lifetime PSD95 synapses | We repeat what is shown in Fig. 2 and Fig. 3 for short-lifetime PSD95 synapses. (a) Coronal view of short-lifetime PSD95 synapses. (b) Absolute correlation coefficient (Spearman's r) between all time-series features and short-lifetime PSD95 synapse density. Green points are statistically significant ($p < 0.05$ after Bonferroni correction). Top features are all related to model forecasting. (c) Scatter plots showing the correlation between short-lifetime PSD95 synapse density (x -axis) and weighted in-degree of SC, weighted out-degree of SC, and weighted degree of FC. Each point is a brain region, and points are coloured according to major ontological structure.

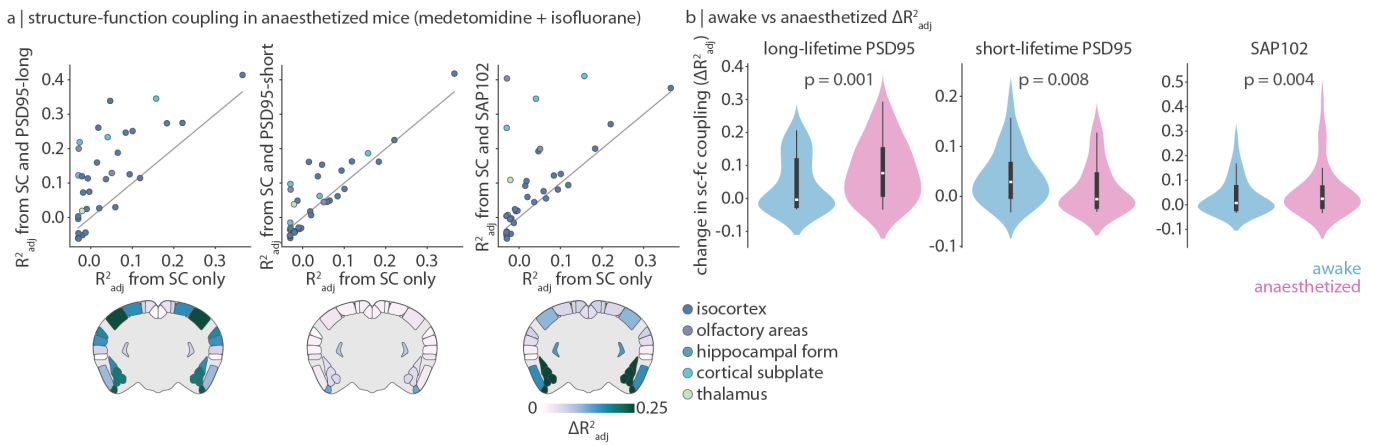


Figure S5. Synapse type density improves structure-function coupling | Structure-function coupling analysis in Fig. 4 was repeated using a functional connectome from mice anaesthetized with medetomidine and isoflurane. (a) Structure-function coupling before (x -axis) and after (y -axis) adding synapse type density (long-lifetime PSD95, short-lifetime PSD95, and SAP102) to the model. Each point is a brain region, and points are coloured according to major ontological structure. The identity line is shown in grey. Coronal slices show the change in coupling (ΔR^2_{adj}) after adding synapse density to the model. Data are mirrored across hemispheres for visualization. (b) We compare the change in structure-function coupling (distribution of ΔR^2_{adj}) in awake versus anaesthetized mice, for all three synapse types separately. Statistical significance is assessed using a two-sided dependent non-parametric t-test for paired samples (Wilcoxon signed-rank test). Violin plots estimate a kernel density on the underlying data, the white point represents the median, the thick vertical line represents the quartiles of the distribution, and the thin vertical line represents the range.

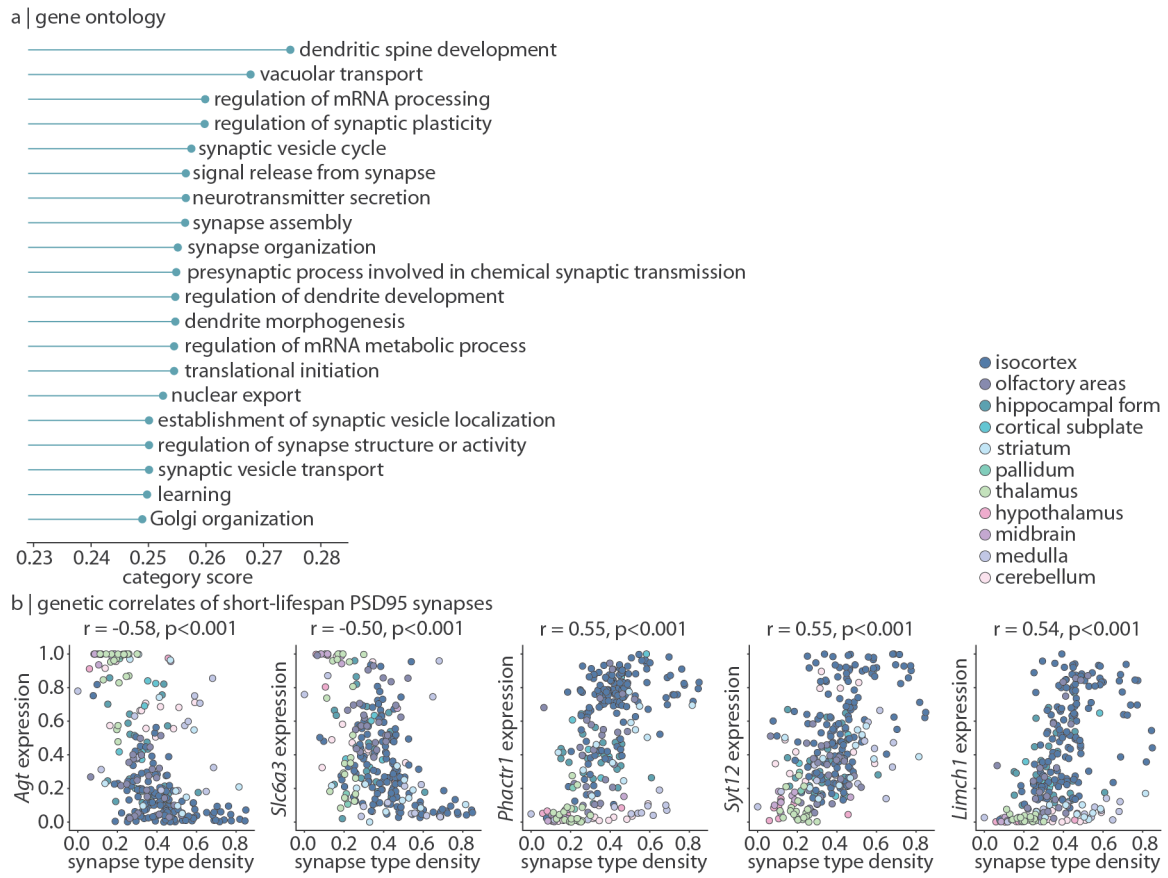


Figure S6. Transcriptomic profile of short-lifetime PSD95 synapses | We repeat what is shown in Fig. 5 for short-lifetime PSD95 synapses. (a) For each of 1616 biological process categories associated with at least 100 genes, we calculate the median absolute correlation (Spearman's r) between short-lifetime PSD95 synapse density and all genes in the category ("category score", x -axis). The top 20 category scores for each synapse type are shown. (b) Selected genes whose expression is highly correlated (Spearman's r) with short-lifetime PSD95 synapses. Each point is a brain region, and points are coloured according to major ontological structure.

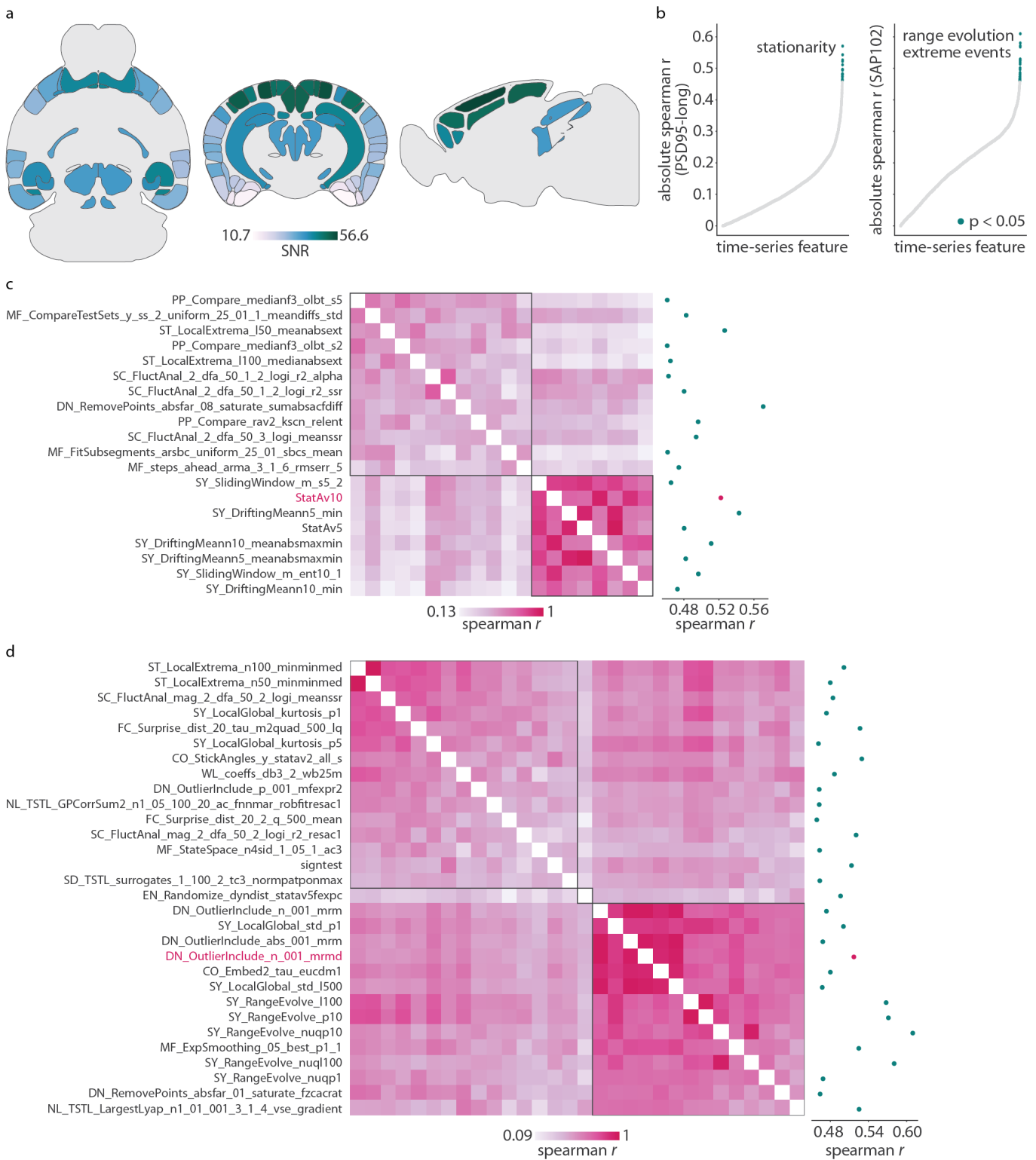


Figure S7. Signal-to-noise ratio of fMRI signal in awake mice | (a) Signal-to-noise ratio (SNR) is calculated as the mean signal within a region divided by the standard deviation of the signal outside of the brain. SNR is shown on a coronal, axial, and sagittal slice. (b) SNR-regressed time-series features were recorrelated with long-lifetime PSD95 and SAP102 synapse density. Green points are statistically significant ($p < 0.05$ after multiple comparisons correction). (c)–(d) For all features that are significantly correlated with long-lifetime PSD95 synapse density (c) or SAP102 synapse density (d) (after SNR regression), we generate a feature \times feature similarity matrix. The scatter plot on the right shows the correlation between each feature and synapse density. The highlighted feature represents that which was mentioned in the main text and in Fig. S2, Fig. S3.

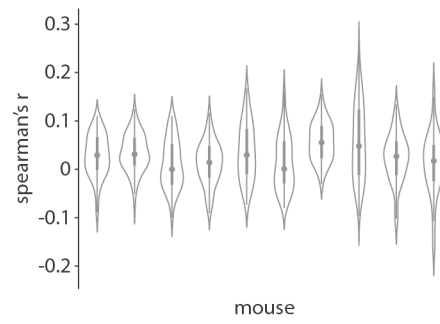


Figure S8. Relationship between signal amplitude and frame-wise displacement | For each mouse, we correlate regional signal amplitude (88 regions) with frame-wise displacement (FD), that is, the amount of motion between any two consecutive time-points. Violin plots estimate a kernel density on the underlying data (88 correlation coefficients). The circle represents the median, the thick vertical line represents the quartiles of the distribution, and the thin vertical line represents the range.



Figure S9. Relationship between synapse type density and cell density | For each synapse type (y -axis), we correlate its spatial distribution with the density of 9 different cell types (x -axis) []. Asterisks represent statistically significant associations (Bonferroni-corrected $p < 0.05$).